Heliyon 9 (2023) e13098

Contents lists available at ScienceDirect

Heliyon

journal homepage: www.cell.com/heliyon

Research article

Spatio-temporal analysis of urban heat island (UHI) and its effect on urban ecology: The case of Mekelle city, Northern Ethiopia

Solomon Tesfamariam [a,b,*], Vanum Govindu [a], Abera Uncha [a]

[a] Department of Geography and Environmental Studies, Arba Minch University, Ethiopia
[b] Institute of Paleo-environment and Heritage Conservation, Mekelle University, Ethiopia

ARTICLE INFO

Keywords:
Dry bare soil
Built-up
Impervious surface
Urban Heat Island
Urban thermal variance

ABSTRACT

The bio-geophysical effects of land cover classes are considered to be an important factor in land surface temperature variations between urban and suburban areas. This means that major cities are significantly warmer than surrounding suburban or rural areas, which is known as the Urban Heat Island (UHI) effect. The aim of this study was to assess and analyze the spatiotemporal variation, correlation and impact of UHIs on Mekelle city (1990–2020) using remote sensing techniques. The study's primary objective was accomplished using the a number of techniques, including the extraction of LULC classes, estimation of the seasonal LSTs, assessment of UHI and UTFVI, and showing the relationship between LULC and LST as well as the interactions between UHI, UTFVI, and urban LULC classes. By analyzing TIRs/OLI thermal band data after calibrating uncertainty in the images and validating it using the concept of theoretical relationships and least squares fitting method, estimates of local LST, UHI (both in Mekelle and periphery rural areas), and UTFVI were obtained. The result of standard multiple regression models showed that impervious urban land surface, built-up areas, and dry bare soil highly contribute and influence variation at LST intensity caused for the formation of UHI in the study area. The result showed that the maximum UHI value in Mekelle city was 2.73 °C during the dry season in 1990. It decreased slightly to 2.53 °C in 2000 and then increased regularly to 2.83 °C and 2.98 °C in 2010 and 2020, respectively. To determine the city's UHI status in comparison to eight selected peripheral suburban areas, a trend analysis has been done. The UHI intensity of Mekelle city was higher relatively to that of most of the periphery suburban districts, particularly in 2020 (both dry and rainy seasons); this could be due to the city's explosive growth. It's worth noting that the research area affected by the urban heat island effect has grown over time, and as a result, the study area also has severe microclimate conditions that primarily damage the quality of urban life and create the worst conditions for thermal discomfort. The results of this study provide major conceptual understandings of how improper distribution and use of urban land affects the urban environment and fuels the creation of the UHI and thermal discomfort phenomena. Hence policy makers and urban planners should consider the effects of LST and UHI and integrate UHI comprehensive mitigation strategies with urban development patterns, and current and projected local climate changes in order to create sustainable urban environments, cities, and communities. In conclusion, compared to the conventional method, satellite remote sensing provides a faster and more efficient method for researching LST and UHI.

* Corresponding author. Department of Geography and Environmental Studies, Arba Minch University, Ethiopia.
E-mail addresses: solomon.tesfamariam@mu.edu.et (S. Tesfamariam), govindu_gis@yahoo.com (V. Govindu), abera.uncha@amu.edu.et (A. Uncha).

https://doi.org/10.1016/j.heliyon.2023.e13098
Received 20 June 2022; Received in revised form 12 January 2023; Accepted 16 January 2023
Available online 26 January 2023

1. Introduction

The term "urbanization" refers to both an increase in the proportion of the population living in cities and the physical expansion of already existing urban centers [1]. Africa has a low level of urbanization (37.1%) when compared to developed countries such as Europe (72.7%) and North America (79.1%). However, urbanization is accelerating much faster in the developing world as a whole than in developed countries, where rates of growth can reach 3% or 4% per/year [2]. Rural-urban migration, economic growth and development, technological change, and rapid population growth are all factors contributing to rapid urbanization in the developing world [3].

Ethiopia is one of the world's least urbanized countries; only 16% of its population lives in urban areas. However, given the annual population growth rate of 2.73%, the high rate of in-migration to towns and the increase in the number of urban centers, the rate of urbanization is increasing at a rate of 4.4% [4]. Furthermore, the UN-Habitat report released in 2019 stated that by 2050, 42.1% of the nation's population will reside in urban areas, with an average annual growth rate of 3.98%. One of the most crucial effects of urbanization is the change in urban land use and land cover classes (LULC). Impervious land cover classes, usually known as infrastructure which has a substantial impact on land surface temperature (LST), have mostly replaced vegetative cover such as woods, grasslands, and croplands [5]. Urbanization related changes in LULC have been demonstrated to have a major impact on the nearby local climate over the past several years [6]. Along with other climate indicators, the LST is a crucial indication and predictor of the metropolitan climate and is susceptible to physical influences like vegetation density, soil moisture, and snow cover [7].

Various scholars argue that changes in land use and unplanned utilization of urban land classes' cause an increase in LST. This research is focused on shifts in LULC that have been reported by Wilby [8] in London, Yuan et al. [9] in Shanghai, Oluseyi et al. [10] in Kogi State, Nigeria, Meng et al. [11] in Beijing, Teferi and Abraha [12] in Addis Abeba, and Sisay and Korme [13] in Hawassa city. Rapid and unplanned urbanization is primarily the result of increased changes in urban land use (LU) and urban land surface temperature (LST), which contribute significantly to the formation of urban heat islands (UHI) and have negative effects on human well-being (health and livelihood conditions), physical and biological environmental resources, and environmental rehabilitation programs [[14–16]].

Urban heat islands (UHIs) are defined as phenomena/events that occur when air and surface temperatures in urban areas are significantly greater than those in suburban areas nearby [5]. The bio-geophysical effects of land cover classes are considered to be the main factor responsible for the variation in surface temperature between urban and suburban areas. This means that a metropolitan area is significantly warmer than surrounding peripheral or rural areas, which is referred to as an UHI. Howard initially introduced the concept of UHI in 1820; later, in the 19th and 20th century, in Paris and Vienna, respectively, Emilian Renou and Wilhelm Schemidt investigated the concept [17]. The change in underlying surface properties leads to a temperature difference between urban and rural areas, but this does not mean that the contribution of geological events and dynamics on atmosphere chemistry is insignificant. Essentially, geological processes resulting from the presence of young magmatic rock bodies or hot rocks located deeper in the crust are one of the main reasons for the formation of natural heat islands in active volcanic areas such as rift and ring belt zones [18]. In these areas, heat can often be transferred to the earth's surface during a volcanic eruption via the conduction of rocks, water, and other associated minerals and can manifest at the surface in the form of hot springs, fumaroles, and heated soils [19].

In fact, a number of factors, like a loss of vegetation, a high water impermeability of structures, or the materials used in roadway paving, favor the formation of UHIs in urban settings. Aside from that, the nature of these building materials and residents' regular activities may result in anthropogenic heat, air pollution, and lower wind speeds [20]. However, the concentration and formation of UHIs phenomena are closely associated to high intensity of LST triggered by dynamics of LULC [16]. It has also contributed to a number of environmental changes such as regional climate, vegetation growth, and water and air quality. These factors, in turn, intensely affect people's health and well-being and can potentially lead to increases in morbidity and mortality, digestive system diseases, nervous system diseases (insomnia, irritability, depression, and memory loss), energy consumption, and even violent incidents in urban areas [20].

Surface urban heat islands (SUHIs), also characterized to as radiative temperature differences between impervious and pervious/natural surfaces, are more pervasive during the daytime when the sun is shining. Seasonally, the magnitude varies, but summer is typically when it reaches its maximum [21]. SUHIs are primarily observed through remote sensing in the thermal infrared (TIR) region of the electromagnetic (EM) spectrum. The relationship between urban land uses and urban heat is still detected and understood through remote sensing [22]. Remote sensing, enables the study of the urban thermal environment at various spatial (from local to global) and temporal (diurnal, seasonal, and inter-annual) scales [[15,23]]. TIR wavelengths ranging from 8 to 15 μm (μm) are commonly used for LST estimation. The radiance emitted by the earth's surface and top atmosphere (TOA) is measured using satellite TIR sensors. However with air attenuation (water vapor and aerosols), the angle at which a satellite sensor receives the radiation, atmospheric pollution, and surface emissivity (built-up areas, vegetation, bare soil, etc.) affects TOA radiances. Relatively low infrared radiation (IR) that the land surface emits is absorbed by the atmospheric window between 10 and 12 μm. Meanwhile, LST is calculated in this spectral range using one or more IR bands [[5,24–28]].

The impact of UHI can be quantitatively described and assessed by various indices of thermal comfort. These include the temperature-humidity index (THI), physiological equivalent temperature (PET), the Wet-bulb globe temperature (WBGT), and urban thermal field variance index (UTFVI) [29]. Several studies have successfully used the UFTVI to evaluate the impact of SUHI intensity on thermal and ecological environmental conditions based on LST [30]. UTFVI has an advantage over other indicators because it exclusively uses thermal satellite data, which enables it to provide a large-scale urban proxy value for SUHI impacts at the pixel resolution level as well as a categorical ecological rating scale for rapid assessments of the quality of the global urban thermal

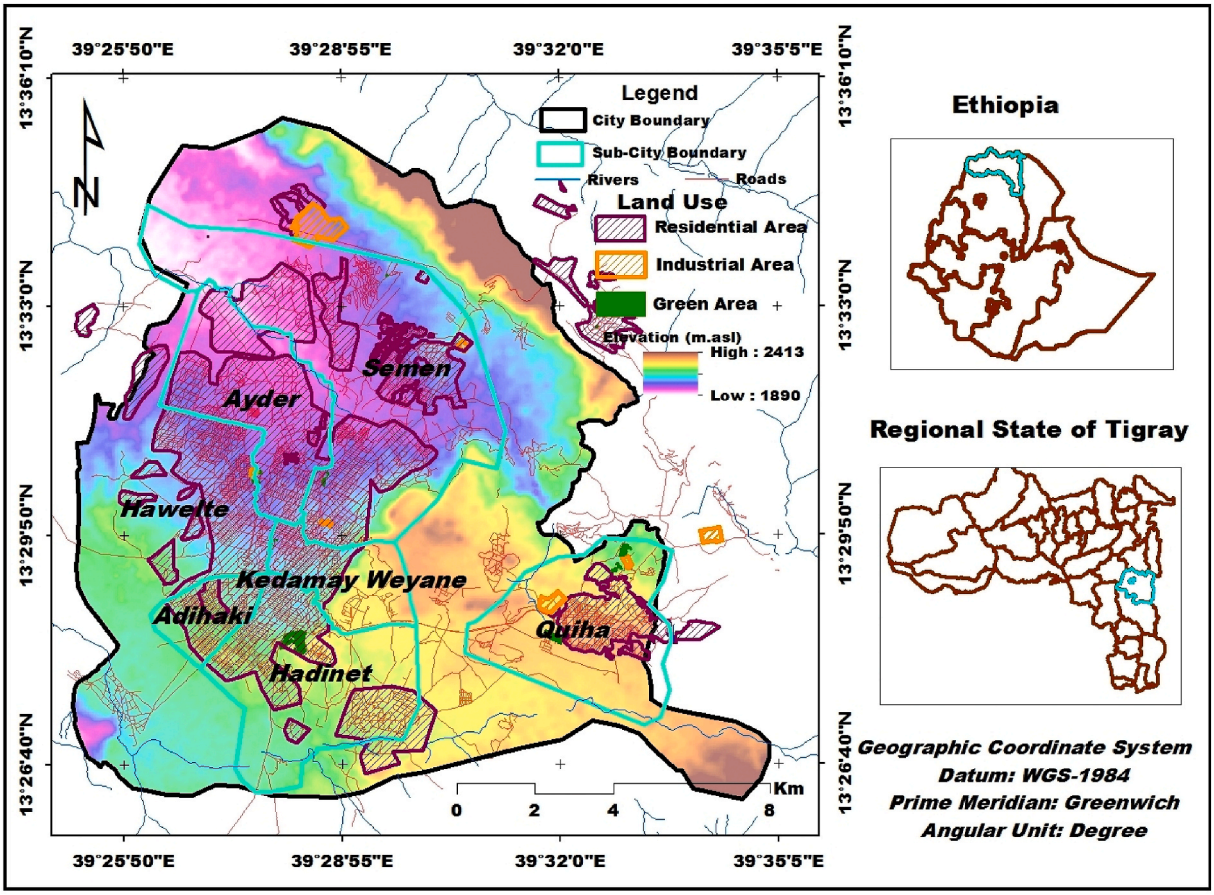

Fig. 1. Map of the study area.

environment with extended, demonstrated reliability across various climatic regions and urbanization [31]. The energy balance impacts produced by the various land classes and their geographical distribution in the urban area have an impact on how strongly SUHI consequences are perceived [32].

The concentration of UTFVI is higher and much warmer in urban areas than in neighboring rural areas due to human activities [20]. UTFVI has significant negative impacts on local wind patterns, humidity, air quality, indirect economic losses, lower comfort, and higher mortality rates [33]. Urbanization causes in urban land cover change (ULCC), which has a substantial impact on local land surface temperature (LST), tends to produce pollution [34], deteriorates air and water quality, and leads in UHI [35].

Impressive studies have been conducted on UHIs and the characteristics, causes, impacts, and remedies they provide. For instance, Gala et al. [36] study on the ecological assessment of UHI occurrences in Chicago and reported a significant correlation between the normalized difference built-up index (NDBI) and the normalized difference vegetation index (NDVI). Kafy et al. [37] empirically verified, evaluated, and forecast the seasonal UTFVI and UHI of Cumilla, Bangladesh's. Nuruzzaman [38] also elaborated the causes, effects, and solutions of UHI effects. In a comprehensive review of the consequences of UHI intensity in East African urban areas, Li, Stringer, and Dallimer [39] also explored the effects of topography and building or construction materials. Similar to the aforementioned studies; Sisay & Korme [13], also conducted studies on the cause of UHI in Hawassa city, Ethiopia and try to mention the contribution of geological processes essentially resulting from the presence of young igneous bodies or hot rocks near the city.

Ethiopia, particularly Mekelle, the nation's second-largest city, has gained insignificant attention or perhaps uncovered despite the fact that UHIs and related issues have been explored in many parts of the world. Due to the crucial role that urbanization played in the establishment of UHI and its consequences on human well-being, urban managers, planners, and policymakers needed substantial and quantifiable data to understand what was/is happening and predict the scenario in the near future. This enabled us to address the following inquiries: (1) how does LST relate to the key variables NDVI, BCI, DBSI, EBBI, MNDWI, and DEM? (2) Which factors are most effective at predicting LST? (3) How do UHI vary spatio-temporarily in Mekelle City and its environs? And what are some potential driving factors? Thus, the aim of this study was to assess and analyze the spatiotemporal variation, correlation and impact of UHIs on Mekelle city (1990–2020) using remote sensing techniques. Moreover, this study will be crucial in filling the research and data processing gap at the regional level.

Table 1
Description data type and source.

Year	Sensor	Season	Date Acquisition	Path/Raw	Band Resolution (m)	Cloud Cover (%)
1990	LandSat-5 TM	Rainy	Sep 15, 1990 Oct 15, 1990 Dec 18, 1990	168/051 168/051 168/051	30	0.00 0.00 0.00
		Dry	Feb 24, 1990 May 15, 1990	169/051		1.00 1.00
2000	LandSat-5 TM	Rainy	Sep 27, 2000 Nov 02, 2000 Dec 27, 2000	168/051 169/051 168/051	30	1.00 1.00 1.00
		Dry	Feb 02, 2000 Mar. 16, 2000 May 19, 2000	168/051	30	1.00 1.00 1.00
2010	LandSat-7 ETM	Rainy	Sep 28, 2010 Nov 30, 2010 Dec 01, 2010	168/051	30	6.00 1.00 0.00
		Dry	Feb 16, 2010 Mar 27, 2010 Apr. 05, 2010	168/051 169/051 168/051	30	4.00 1.00 0.00
2020	LandSat-8 OLI	Rainy	Sep 22, 2020 Nov 11, 2020 Dec 12, 2020	169/051 168/051 168/051	30	3.03 2.08 0.26
		Dry	Mar 07, 2020 Apr. 08, 2020 May 26, 2020	168/051	30	0.00 0.00 0.60

Table 2
Description of Mean Air temperature in ten year interval (^{O}C).

Station	Year	January–May		June–August		September–December		Mean Annual		
		Max	Min	Max	Min	Max	Min	Max	Min	Mean
Mekelle Airport	1980–1990	27.7	16.5	28.5	24.5	26.1	17.8	27.5	19.7	23.6
	1991–2000	26.1	16.9	28.8	24.2	26.8	17.6	27.2	19.6	23.5
	2001–2010	28.2	17.6	28.8	24.9	26.5	18.6	27.8	20.4	23.9
	2011–2020	28.7	17.9	28.8	25.2	26.9	19.2	28.1	20.7	24.3

Source: - Ethiopia Meteorological Agency and https://gis.ucar.edu/gis-climatedata. N.B. Min (Minimum mean Temperature), Max (Maximum mean Temperature)

2. Materials and methods

2.1. Description of the study area

Mekelle is one of the most influential and the second largest city and business center in the Northern part of Ethiopia. The establishment and the local history of Mekelle city was date back to the 14th century A.D [40]. Mekelle is located between 39°26′60″ to 39°35′5″E and 13°26′40″ to 13°33′0″N, with an average elevation of 2151 m/a/sl (Fig. 1).

The land use and elevation map of the study area was extracted and derived from (https://www.openstreetmap.org/) and ASTER digital elevation model (DEM), downloaded from USGS (http://earthexplorer.usgs.gov) respectively. Mekelle is the capital of Tigray Regional State in the Northern part of Ethiopia, spatially it was covered around 2304 ha in the early 1990s, now it covers an area of 19,682.19 ha and is divided into seven sub-cities namely; Quiha, Adi Haqi, Kedamay Weyane, Hadinet, Hawelti, Ayder, and Semien sub cities. The population is approximately 524,000 with an increasing rate of 3.76% from 2019. Being a capital of Tigray Regional State, economic, business, industries, and tourism hub of the regional state therefore a considerable amount of migration took place in the city which caused for rapid population growth and urbanization.

2.2. Data source

30-m cloud-free Landsat TM, ETM+ and OLI sensor satellite image of the rainy season (September to December) and dry season (March to May) of 1990, 2000, 2010, and 2020 are downloaded from USGS (http://earthexplorer.usgs.gov). The aforementioned months have been selected depending on the local weather conditions and availability of optimum cloud-free/fewer satellite imageries which is best for estimation of thermal LST and spectral index analysis. An average seasonal LST was produced to solve the problem of comparing LST values from different days (Table 1) and data on air temperature was obtained from the Ethiopian metrology agency (Table 2).

2.3. Method

To achieve the objective of the study, several methods were used, such as extracting LULC classes, estimating the spatial pattern of seasonal LST, assessing UHI and UTFVI and showing the relationship between LULC and LST and spatio-temporal pattern and linkage between UHI, UTFVI and urban LULC classes. Urban land use classes were extracted using spectral induces threshold value and validated by accuracy assessment of randomly collected 180 (20 for water bodies and 160 for other LULC) GCP data. Estimation of local LST, UHI (both in Mekelle and peripheral rural areas) and UTFVI was obtained by analyzing TIRs/OLI thermal band data after calibrated uncertainty in the images [41] and validated by the concept of theoretical relationships and least squares fitting method. Pixel-based correlation and standard regression models were run to determine the relationship and relative causation of LST occurrence. Before running the model, some redundant thresholds from all reclassified spectral index LULC classes were masked to minimize overestimation and representation of LULC classes. Then, the data were resampled to the same cell size (30 × 30 m) and converted to point data, which were used as input variables in the correlation and regression model. Therefore, only the urban LULC classes covered with vegetation *(rare, medium, and dense vegetation),* water bodies, impervious surfaces *(dark and bright impervious)*, dry bare soil, and

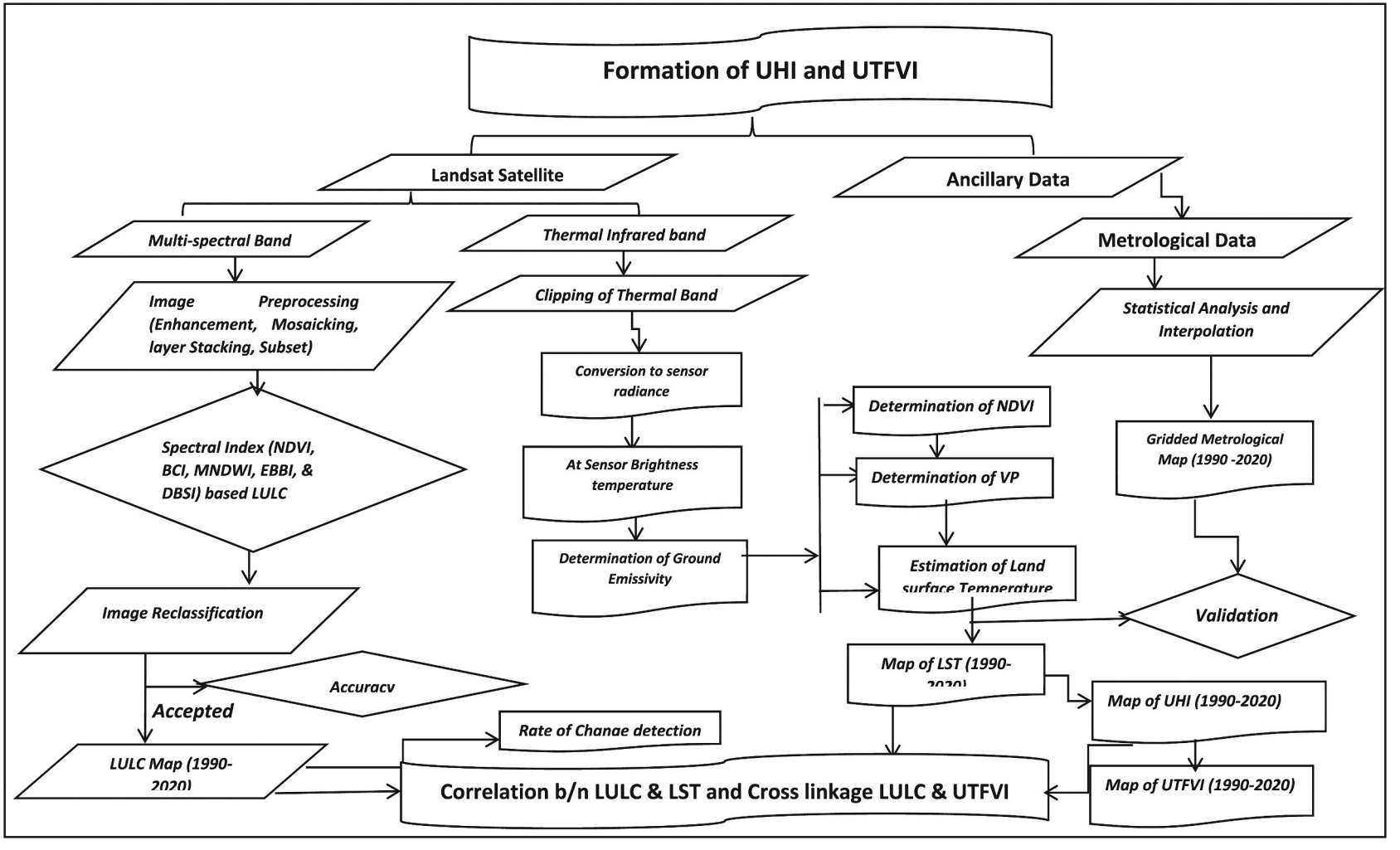

Fig. 2. Schematic flow chart of the extraction and comparison method.

Table 3
Summery of ecological evaluation index (EEI) threshold value.

EEI	UTFVI	UHI	Source
Excellent	<0	None	[42]
Good	0.000–0.005	Weak	
Normal	0.005–0.010	Middle	
Bad	0.010–0.015	Strong	
Worse	0.015–0.020	Stronger	
Worst	>0.020	Strongest	

EEI (Ecological Evaluation Index), UTFI (Urban thermal field variance index), UHI (Urban Heat Island).

Table 4
Summery of NDVI based land use spectral index threshold value.

Input Surface Reflectance Value (μm) [43]								
LU/LC	Year:- 1990		Year:- 2000		Year:- 2010		Year:- 2020	
	Dry Season	Wet Season	Dry Season	Wet Season	Dry Season	Wet Season	Dry Season	Wet Season
RV	0.01–0.32	0.14–0.44	0.16–0.45	0.16–0.44	0.15–0.42	0.14–0.44	0.14–0.41	0.22–0.41
MV	–	0.44–0.65	0.45–0.65	0.44–0.67	0.42–0.64	0.44–0.64	0.41–0.66	0.41–0.65
DV	–		-		-	-	-	-

N.B. RV (Rare Vegetation), MV (Medium Vegetation), & DV (Dense Vegetation).

Table 5
Summery of MNDWI based land use spectral index threshold value.

Input Surface Reflectance value (μm) [44]								
LU/LC	Year:- 1990		Year:- 2000		Year:- 2010		Year:- 2020	
	Dry Season	Wet Season	Dry Season	Wet Season	Dry Season	Wet Season	Dry Season	Wet Season
WB	−0.03–0.62	−0.03–0.60	−0.13–0.58	−0.02–0.99	−0.07–0.48	0.03–−0.42	−0.02–−0.22	−0.27–0.01

WB (Water body).

Table 6
Summery of BCI based land use spectral index threshold value.

$$DBSI = (\rho(SWIR) - \rho(Green)) / (\rho(SWIR) + \rho(Green)) - NDVI \quad (7)$$

Input Surface Reflectance Value (μm) [45]				
LU/LC	**Year:- 1990**	**Year:- 2000**	**Year:- 2010**	**Year:- 2020**
Dark Impervious	0.02–0.05	−0.21–−0.16	−0.08–0.01	0.02–0.14
Bright Impervious	0.05–0.13	−0.16–0.14	0.01–0.99	0.14–0.99

Table 7
Summery of DBSI based land use spectral index threshold value.

Input Surface Reflectance Value (μm) [47]								
LU/LC	Year:- 1990		Year:- 2000		Year:- 2010		Year:- 2020	
	Dry Season	Wet Season	Dry Season	Wet Season	Dry Season	Wet Season	Dry Season	Wet Season
DB	0.37–0.59	0.32–0.77	0.41–0.65	0.39–0.87	0.45–0.59	0.36–0.61	0.12–0.31	0.07–0.37

DB (Dry Bare Soil).

built-up features were extracted from the NDVI, MNDWI, BCI, DBSI, and EBBI spectral indices, respectively (Fig. 2). The estimated UTFVI values were classified into six categories (None, Weak, Moderate, Strong, Stronger, and Strongest) based on the fixed ecological evaluation index (EEI) threshold value (Table 3) to describe the urban health and heat distribution in the study area [42]. The observed LST and UHI of Mekelle city were blindly compared with the eight selected peripheral districts *(Ara'to, Debri, Hebite (Shibta), Mesebo, May Alem, May Tsea'da, May Anbesa, and Mahidere Genet)* chosen for their geographical proximity (Fig. 7). Finally, tabular cross linkage method was applied to determine the significant influence of UHI and UTFVI phenomena on the urban ecology.

Table 8
Summery of EBBI based land use spectral index threshold value.

Input Surface Reflectance Value (μm) [48]				
LU/LC	**Year:- 1990**	**Year:- 2000**	**Year:- 2010**	**Year:- 2020**
Built up	0.14–0.35	0.12–0.35	0.17–0.37	1.11–0.36

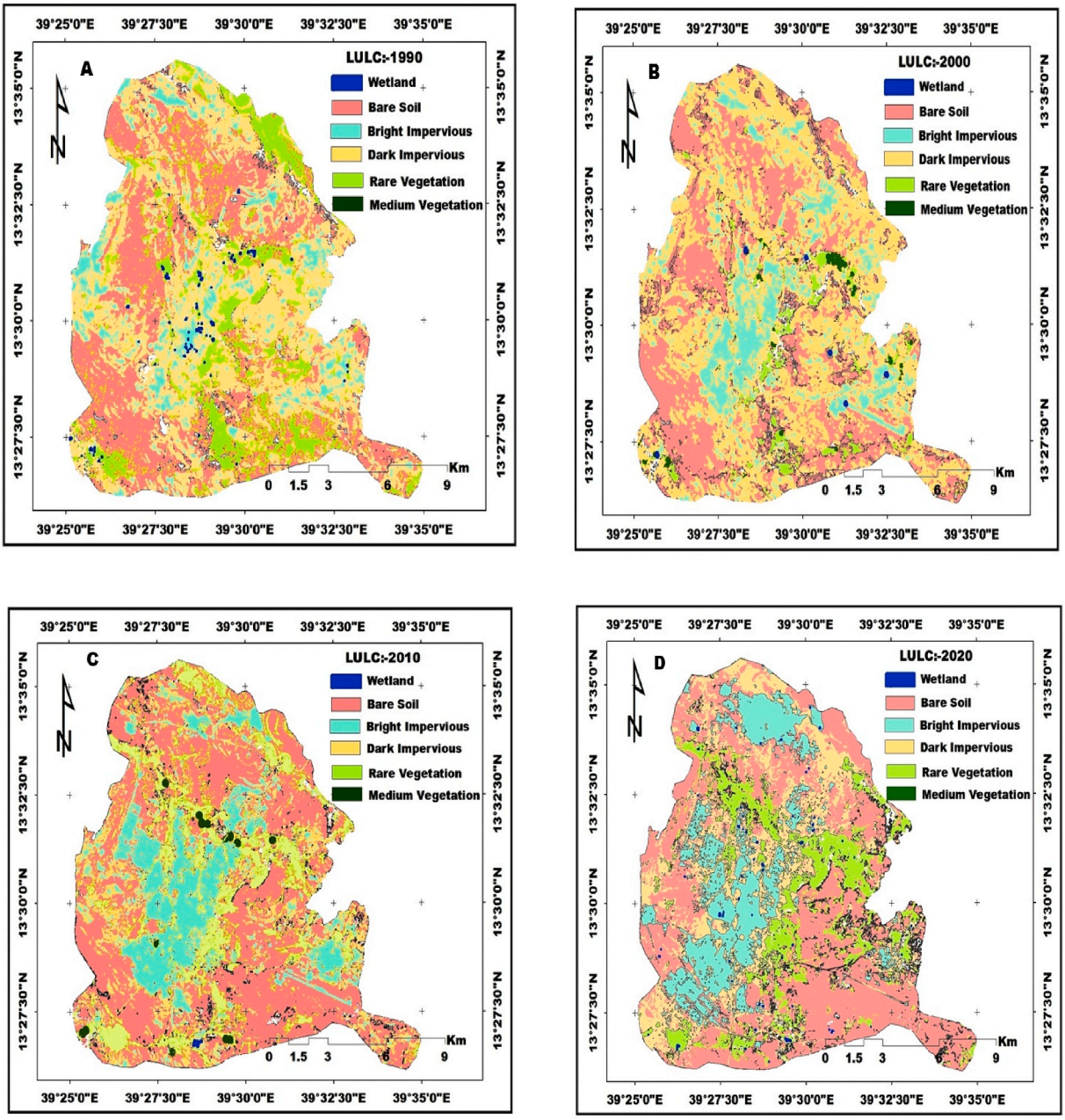

Fig. 3. Dry season distribution pattern of Urban Land Cove (A) 1990, (B) 2000, (C) 2010 & (D) 2020.

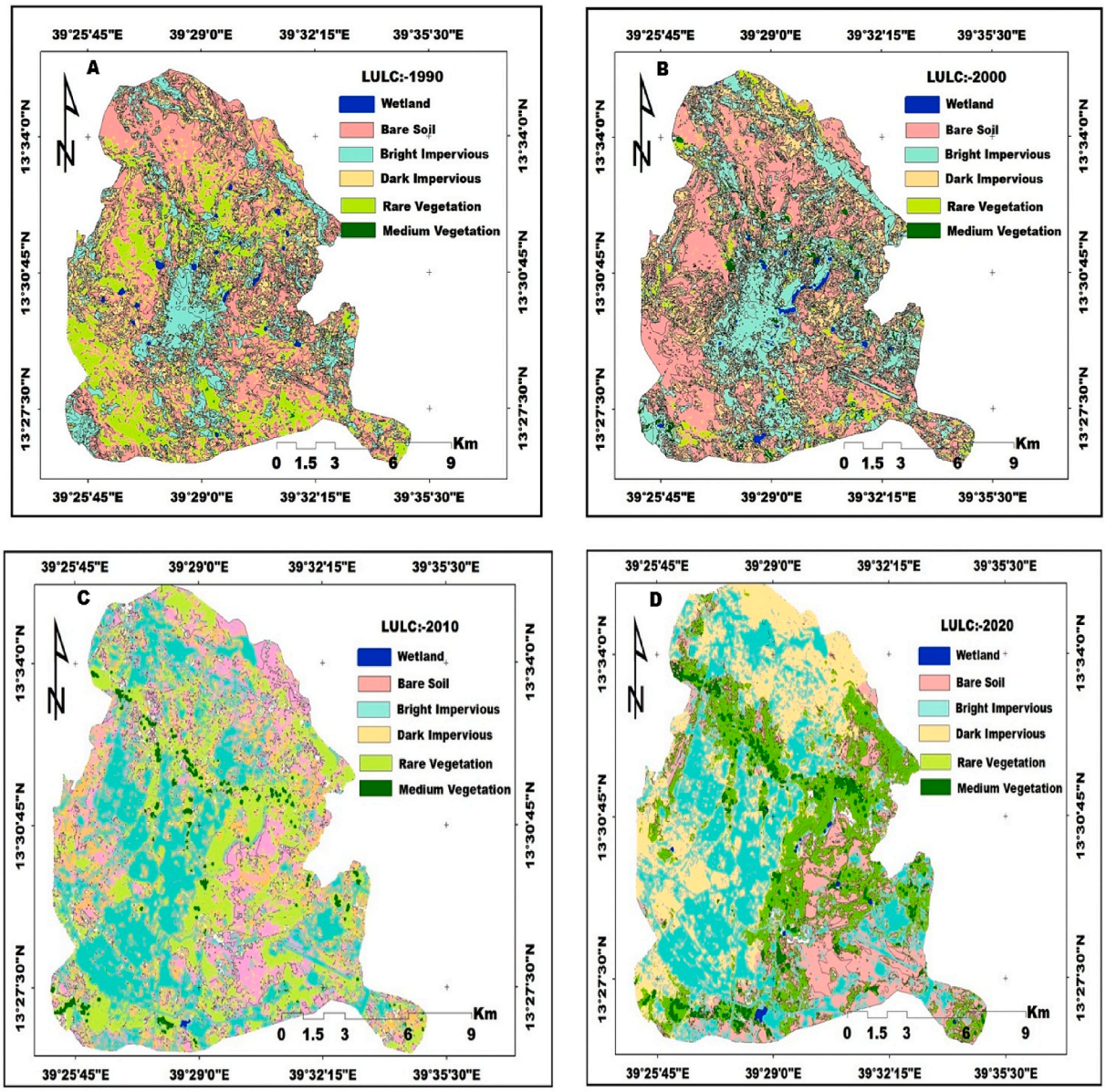

Fig. 4. Wet season distribution pattern of Urban Land cove (A) 1990, (B) 2000, (C) 2010 & (D) 2020.

2.3.1. *Urban land cover mapping*

A spectral index-based NDVI (Eq. (1)), MNDWI (Eq. (2)), BCI (Eq. (3)), DBSI (Eq. (7)), and EBBI (Eq. (8)) method was applied to classify the satellite images of the study areas into five lands cover categories such as; vegetation, water body, impervious surface, bare land, and built up features. After reclassified the spectral index, masked the urban land classes using a threshold value (Tables 4–8) and therefore, only the urban LULC classes covered with dense vegetation, medium vegetation, rare vegetation, water bodies, bright impervious, dark impervious, dry bare soil, and built-up features were extracted and develop the spatio-temporal distribution LULC map of the study area in ten years' time interval (Figs. 3–4). The spectral index were developed using the following well known mathematical equations.

$$NDVI = (\rho(\mathrm{NIR}) - \rho(\mathrm{Red}))/(\rho(NIR) + \rho(Red)) \tag{1}$$

where, NDVI, normalized difference vegetation index (Vegetation cover), ρ represents the radiance in reflectance units of near infrared and red bands of the Landsat images [43].

$$\boldsymbol{MNDWI} = (\boldsymbol{\rho}_{Green}) - (\boldsymbol{\rho}_{SWIR} - \mathbf{1}) \,/\, (\boldsymbol{\rho}_{Green} + \boldsymbol{\rho}_{SWIR} - \mathbf{1}) \tag{2}$$

Table 9
Thermal band calibration.

Thermal Band Calibration Constants								
Sensor-ID	Band	Year	K1 ($Wm^{-2}sr$ -1μm)	K2 ($Wm^{-2}sr$ -1μm)	R_{Max} ($mW \times cm^{-2} \times sr^{-1}$)	R_{Min} ($mW \times cm^{-2} \times sr^{-1}$)	M_P Value	A_P Value
LandSat-5TM	6	1990 & 2000	607.76	1260.56	15.303	1.238	$5.5375E^{-02}$	1.18243
LandSat-8TM	10 & 11	2010	774.8853	1321.0789	22.0018	0.1003	$3.3420E^{-04}$	0.10
	10	2020	480.8883	1201.1442	22.0018	0.1003	$3.3420E^{-04}$	0.10
	11	2020	774.8853	1321.0789	22.0018	0.1003	$3.3420E^{-04}$	0.10

K_1 & K_2 (Constant Band), R-Max & R-Min (Radiance Maximum& Minimum), M_P & A_P *(Reflectance multiplicative & additive scaling factor for the band).*

where, MNDWI, modified normalized difference water index (open water surface), ρ represents the radiance in reflectance units of green and short wave infrared bands of the Landsat image [44].

$$BCI = (H + L)/2 - V/(H + L)/2 + V \tag{3}$$

where BCI, Biophysical composition index (Impervious Surface), H is "high albedo", the normalized TC_1; V is "vegetation", the normalized TC_2; and L is "low albedo", the normalized TC_3. The BCI model [45] was running after calibrating the TIR bands and masked the water using the tasseled cap transformation [46]. H, V and L can be describe as follow,

$$H = C_1 - TC_{1\ Min}/TC_{1\ Max} - TC_{1\ Min} \tag{4}$$

$$V = TC_2 - TC_{2\ Min}/\ TC_{2\ Max} - TC_{2\ Min} \tag{5}$$

$$L = TC_3 - TC_{3\ Min}/TC_{3\ Max} - TC_{3\ Min} \tag{6}$$

where T_{ci} (I = 1, 2 and 3) represent the first three Tasseled Cap transformation, T_{cimin} and T_{CiMax} are the minimum and maximum value of the i_{th}Tc component respectively.*where DBSI, Dry Bare Soil index (Dry bare surface), ρ represents the radiance in reflectance units of short wave infrared (SWIR) and Green bands of the Landsat images* [47].

$$EBBI = (\rho(DN_{SWIR}) - \rho(DN_{NIR}))\ \Big/\ \sqrt{10DN_{SWIR} + DN_{TIR}} \tag{8}$$

where; EBBI represents the enhanced built-up and bareness index (built up feature). ρ represents the radiance in reflectance units, near infrared (NIR) and short wave infrared (SWIR) of TM/ETM + and OLI Landsat image [48].

2.3.2. Estimation of seasonal LST

Landsat images were used to extract seasonal LST for 1990, 2000, 2010, and 2020. Landsat sensors gather thermal data and store them as digital numbers (DNs). The following steps were used for Landsat 5 (Eq. (9)) and Landsat 8 OLI to transform available DNs into LST (Eq. 10- 14).

$$\mathbf{T} = \frac{\mathbf{K2}}{\mathbf{Ln}\left(\frac{\mathbf{K1}}{\mathbf{L_\lambda}} + \mathbf{1}\right)} - \mathbf{273.15} \tag{9}$$

where; T=Effective at-satellite temperature in (^{O}c) of TIRs band of Landsat-5 & 7 [27], *$K_{1\ \&}$ K_2; calibration constant (*Table 9*), L_λ=Spectral radiance in (Watts/(m^2*sr*μm).*

$$\boldsymbol{BT} = \frac{\boldsymbol{K2}}{\boldsymbol{Ln}\left(\frac{\boldsymbol{K1}}{\boldsymbol{L_\lambda}} + \mathbf{1}\right)} \tag{10}$$

where; BT = Top of atmosphere brightness temperature (K) of TIRs band of Landsat-8. [27], *K_1 & K_2 = Band-specific thermal conversion constant from the metadata, L_λ = TOA spectral radiance (Watts/(m^2*srad*μm).*

Ground Emissivity (Ɛv) using NDVI: - The surface temperature for emissivity effect below [41] and the land surface emissivity (LSE) was calculated as (Eq.(11) and (12)) follows [49];

$$Ɛ = Ɛv\ \ * PV + Ɛs\ (1 - PV) \tag{11}$$

$$PV = \frac{NDVI - NDVI_{min}}{NDVI_{max} - NDVI_{min}} \tag{12}$$

where; (Ɛv): emissivity of vegetation (0.99), (Ɛs): emissivity soil (0.986 and PV is proportion of Vegetation.

Estimation of land surface temperature: the value of the brightness temperature (Eq. (10)) was converted to the radioactive

Table 10
Accuracy assessment.

Spectral Index	LULC Class	1990		2000		2010		2020	
		Accuracy	Kappa	Accuracy	Kappa	Accuracy	Kappa	Accuracy	Kappa
NDVI	Vegetation	90.63	0.81	93.00	0.91	88.30	0.85	90.35	0.85
MNDWI	Water body	81.75	0.72	88.30	0.86	82.80	0.73	80.40	0.70
BCI	Impervious surface	92.05	0.79	94.00	0.92	88.30	0.85	86.84	0.80
DBSI	Barren land	87.50	0.77	91.00	0.88	87.78	0.84	92.11	0.87
EBBI	Built-up area	83.70	0.71	91.00	0.88	87.22	0.83	89.47	0.83

NDVI (Normalized Difference Vegetation Index), MNDWI (Modified Normalized Difference Water index), BCI (Biophysical Index), DBSI (Dry Bare Soil Index), EBBI (Enhanced Built-up Index).

surface temperature using the following conversion (Eq. (13)) methods [26].

$$\boldsymbol{LST} = \frac{\boldsymbol{BT}}{\left[\mathbf{1} + \left\{\frac{\lambda \boldsymbol{BT}}{\rho}\right\} \boldsymbol{Ln}\ (\boldsymbol{LSE})\right.} \tag{13}$$

$$\boldsymbol{\rho} = \boldsymbol{h}_{\sigma}^{c} = 1.438 * 10^{-2} mk \tag{14}$$

where; Λ *= is the wavelength of emitted radiance,* P *= was calculated as (Equ.14),* σ *(Boltzmann constant)* $= 1.38 \times 10^{-23}$ *J/K, h (Planck's constant)* $= 6.626 \times 10^{-34}$ *J s, and c (velocity of light)* $= 2.998 \times 10^{8}$ *m/s* [25].

2.3.3. Estimation of seasonal UHI

Therefore, to show the scenarios of UHI (Eq. (15)) in different seasons of the same year, a normalized method was used [50].

$$\boldsymbol{UHI} = \frac{\boldsymbol{T}_{s-T_m}}{\boldsymbol{SD}} \tag{15}$$

where, T_s *stands for LST,* T_m *for the mean of the LST of the study area, and SD for the standard deviation.*

2.3.4. Estimation of seasonal UTFVI

To describe the effect of UHI, evaluation an area's UTFVI (Eq. (16)) was estimated using LST images and mean LST values [37]. The estimated UTFVI values were divided into six categories (None, Weak, Medium, Strong, Stronger, and Strongest) to describe the urban health and heat distribution in the study area [51].

$$\boldsymbol{UTFVI} = \frac{\boldsymbol{T}_s - \boldsymbol{T}_m}{\boldsymbol{T}_m} \tag{16}$$

where, $UTFVI_s$ *Urban thermal filed variance index,* T_s*, Land surface temperature,* T_m*; the mean of the LST of the study area.*

2.3.5. Validity and reliability

The accuracy of the LULC maps was assessed from randomly collected 180 ground data using GPS (for 2020) and data from Google Earth imagery (for 1990–2010). The estimated LST was also validated by the theoretical aspect of correlation with NDVI (Eq. (1)) and EBBI (Eq. (8)) using Pearson correlation [27] and linear least squares method (Eq. (17)) using DEM and mean annual temperature over a period of 10 years [52].

$$\mathrm{LST} = \delta + (\beta * \mathrm{DEM}) \tag{17}$$

Where, δ *stands for LST intercept (constant),* $\boldsymbol{\beta}$ the slope coefficients for the predictor (DEM) values of regression model *and DEM for digital elevation model.*

3. Results and discussion

3.1. Ground truth validation

LULC maps (Figs. 3–4) for the years 1990, 2000, 2010, and 2020 were developed at 10 years interval period from the Landsat data using the automatic spectral index method based on the cut-off threshold value. Each map's accuracy was assessed by randomly collecting 180 ground data using GPS (for 2020) and data from Google Earth images (for 1990–2010). Thus the overall accuracy and the kappa coefficient result (Table 10) demonstrated a good agreement between the classified image and reference data [53].

Pearson pixel-based correlation coefficient also used to validity the estimated LST. Before the execution of the model, the vegetation and built up areas were masked to minimize the overestimation of LULC classes then resampled to the same cell size (30 × 30 m) and converted to point data which was used as input variable data. Theoretically, LST has a positive relationship with the EBBI and negative relationship with the NDVI [27], consequently the result of this study also coincide with the aforementioned theoretical

Table 11
Validation correlation matrix.

Correlation		Year	Dependent Variable	Rainy Season		Dry Season	
				NDVI	EBBI	NDVI	EBBI
Pearson Correlation	1990	LST	−.189**	.199*		−.109**	.175**
	2000	LST	−.395**	.485*		−.039**	.372**
	2010	LST	−.286**	.412*		−.187**	.073**
	2020	LST	−.213**	.585**		−.064**	.503**
N = 213,139							

LST (Land Surface Temperature), NDVI (Normalized Difference Vegetation Index), EBBI (Enhanced Built-up Index).

Table 12
Linear least square.

Year	Mean spatio-temporal distribution of LST (°C)			
	Estimated using TIRs band		Linear Least Square Fitting Method	
	Wet Season	Dry Season	Wet Season	Dry Season
1990	30.01	39.02	30.21	37.99
2000	29.66	37.38	28..69	36.39
2010	27.93	36.26	28.69	36.27
2020	27.96	33.32	27.06	32.72

Table 13
Dry season urban land use coverage and rate of change (1990–2020).

LULC Classes	Area in Hectare				Net Changes 2020–1990	
	1990	2000	2010	2020	Hectare	%
Rare Vegetation	3779.6	718.6	2866.8	3525.2	−254.31	−0.06
Medium Vegetation	–	11.42	1.68	1.49	−9.93	−0.86
Water Body	2.82	4.46	7.64	17.55	+14.7	+5.2
Bright Impervious*	792.13	861.81	1733.7	1409.68	+617.5	+0.77
Dark Impervious*	3910.92	4316.33	5752.29	8007.85	+4096.9	+1.04
Dry Bare Soil	11,200.7	13,774.9	9329.92	6732.47	−4468.2	−0.39
Total Area	**19,685.4**	**19,685.2**	**19,685.9**	**19,685.5**		
Built-up Area*	5212.23	7430.85	8325.73	9892.7	+4680.6	+0.89

N.B:- '-'indicates decrease, '+' indicates increase. The value of Built up excluded in total area.

Table 14
Wet season urban land use coverage and rate of change (1990–2020).

LULC Classes	Area in Hectare				Net Changes 2020–1990	
	1990	2000	2010	2020	Hectare	%
Rare Vegetation	4354.31	2943.14	5748.93	6876.	+2521.69	+0.57
Medium Vegetation	32.78	65.49	59.84	202.79	170	+5.18
Water Body	16.64	26.03	20.12	49.13	+23.1	+0.8
Dry Bare Soil	10,574.4	10,968.9	6384.98	3177.05	−7397.3	−0.69
Total Area	**14,982.2**	**14,005.9**	**12,199.9**	**10,268.1**		

N.B:- '-'indicates decrease, '+' indicates increase.

concept (Table 11.).

In addition, the estimated mean value LST was also validated by the liner least square method (Equ.17) using the daily mean temperature and DEM. The value of LST estimated from the TIRs/OLI satellite imagery most likely agrees with the value derived by the linear least squares method (Table 12).

3.2. Dynamics on urban land cover

The seasonal LULC maps (Figs. 3 and 4) for 1990, 2000, 2010 and 2020 were generated at 10-year intervals from Landsat data using the automated spectral index threshold value and reclassified into six different urban land use classes such as water, rare vegetation, medium vegetation, bright impervious surfaces, dark impervious surfaces, dry bare soils and built-up areas. As shown in the results of the weighted dry season cover comparison study (Table 13), vegetation cover is decreasing between 1990 and 2020. For instance, rare

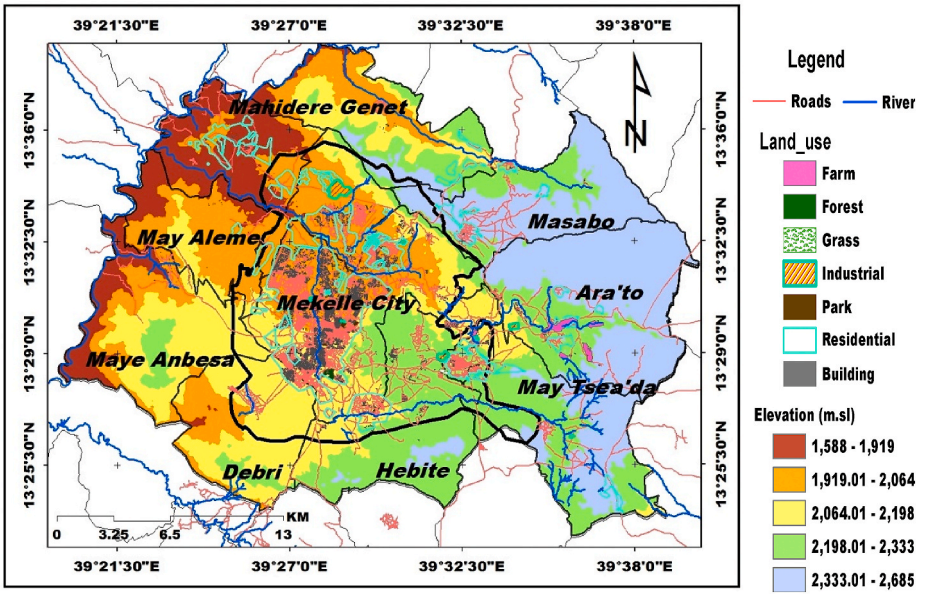

Fig. 5. Map of Mekelle and peripheral urban areas.

Table 15
LST Variation over Mekelle city and Peripheral rural districts (Dry Season).

City/District	Dry Season LST °C								Net Changes 2020–1990 (°C)	
	1990		2000		2010		2020			
	Max LST	Min LST	Max LST	Min LST	Max LST	Min LST	Max LST	Min LST	Δ Max LST	Δ Min LST
Ara'to	39.37	28.19	33.3	24	31.95	15.11	34.8	16.75	−4.57	−11.4
Debri	44.17	28.11	35.4	18.63	33.56	21.42	37.81	24.91	−6.36	−3.2
Hebite *(Shibta)*	43.08	23.17	31.95	16.95	32.62	16.36	36.52	19.83	−6.56	−3.3
Masebo	38.99	28.19	32.21	18.18	31.14	20.1	35.7	23.26	−3.29	−4.93
May Alem	46.75	26.85	37.36	15.44	26.89	10.54	39.59	27.18	−7.16	0.33
May Tsea'da	38.6	26.1	37.7	20	37.71	20.04	34.33	16.91	−4.27	−9.19
May Anbesa	46.38	29.76	36.58	16.36	37.20	10.62	39.72	25.41	−7.19	−4.35
Mahidere Genet	44.91	24.73	38.13	19.52	38.36	10.62	40.21	26.54	−4.7	1.81
Mekelle City	46.38	26.43	44.32	24.03	41.94	22.53	39.53	22.37	−6.85	−4.06

N.B:- '- 'indicates decrease, '+' indicates increase in net Change rate.

Table 16
LST Variation over Mekelle city and Peripheral rural districts (Wet Season).

City/District	Wet Season LST °C								Net Changes 2020–1990 (°C)	
	1990		2000		2010		2020			
	Max LST	Min LST	Max LST	Min LST	Max LST	Min LST	Max LST	Min LST	Δ Max LST	Δ Min LST
Ara'to	35.49	21.36	33.92	19.9	31.76	14.95	33.76	17.53	−1.73	−3.83
Debri	35.11	23.54	33.53	22.06	33.36	21.25	33.99	20.17	−1.11	−3.37
Hebite *(Shibta)*	34.73	22.67	33.14	21.2	31.76	16.78	35.11	19.36	0.41	−3.31
Masebo	35.14	23.11	33.53	21.63	30.95	20.37	34.23	21.97	−0.87	−1.14
May Alem	36.33	21.42	36.33	21.42	35.93	18.76	34.24	19.27	−2.09	−2.15
May Tsea'da	33.51	20.92	31.95	19.46	32.16	14.95	32.46	18.19	−1.05	−2.73
May Anbesa	35.14	20.98	35.14	20.98	32.35	19.20	34.71	20.10	−0.43	−0.88
Mahidere Genet	37.50	23.60	37.50	23.60	37.50	21.42	36.04	22.01	−1.46	−1.59
Mekelle City	36.33	18.31	38.13	16.36	33.6	15.29	34.17	17.52	–2.16	−0.79

N.B:- '- 'indicates decrease, '+' indicates increase in net Change rate.

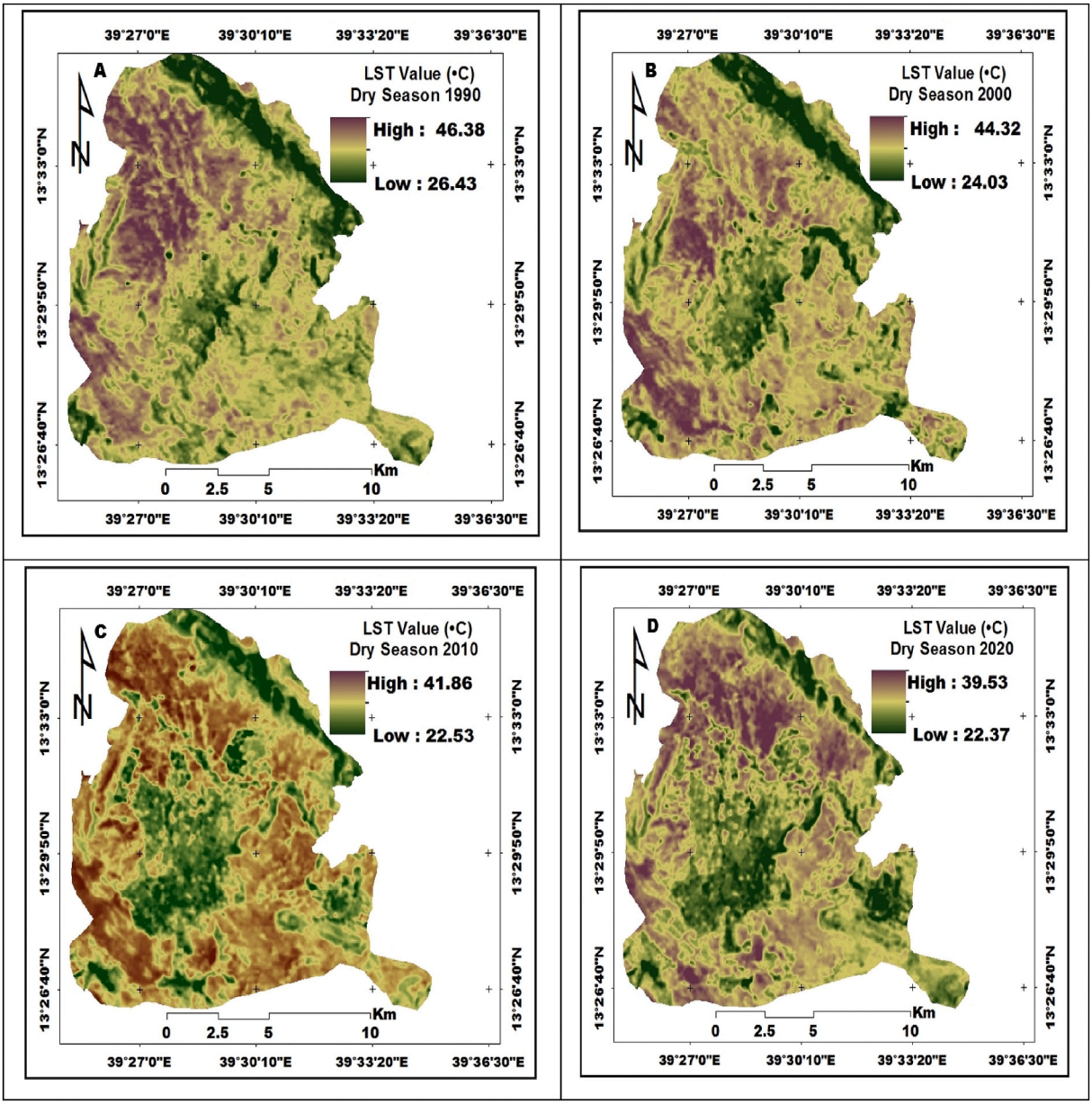

Fig. 6. Dry season average LST map (A) 1990, (B) 2000, (C) 2010 & (D) 2020.

vegetation cover fell from 19.2% to 17.9%. Between 1990 and 2000, medium vegetation cover experienced two transitional phases between 1990 and 2020: a stunning expansion to 0.05% b/n 1990–2000 and a fall to 0.007% with a net change of −0.86% between 2000 and 2020. Furthermore, from 1990 to 2020, rare and medium vegetation increased to 65% and 1.03%, respectively, during the wet season. This is most likely related to conservation and land closure efforts on the hills and slopes of Mount Endayesus, which run along the city's eastern border. Furthermore, increased urban agriculture, particularly in the city's south (east of the airport), and the establishment of the Martyrs Memorial Park in the western portion of the city in 2005 have also contributed to the city's rare vegetation coverage.

The Tekeze basin is traversed by the enduring Elala and Aynalem rivers. The city's southern plain is drained by the Aynalem River, while the city's center (Mekelle) is drained by the Elala River. The city also receives water from a number of seasonal ponds. As with vegetation cover changes, three transitional trends for water body changes were found in both the dry and wet seasons (Figs. 3 and 4): insignificant increase (1990–2000), a significant decline (2000–2010), and a noticeable expansion (2010–2020). Despite certain irregularities in the extent of open water areas, efforts to protect rare vegetation have improved the city's open water spaces (Tables 13 and 14).

According to the estimated BCI value (Fig. 3) of Mekelle city, pervious surfaces dominated 76.1% of the area in 1990, but this has

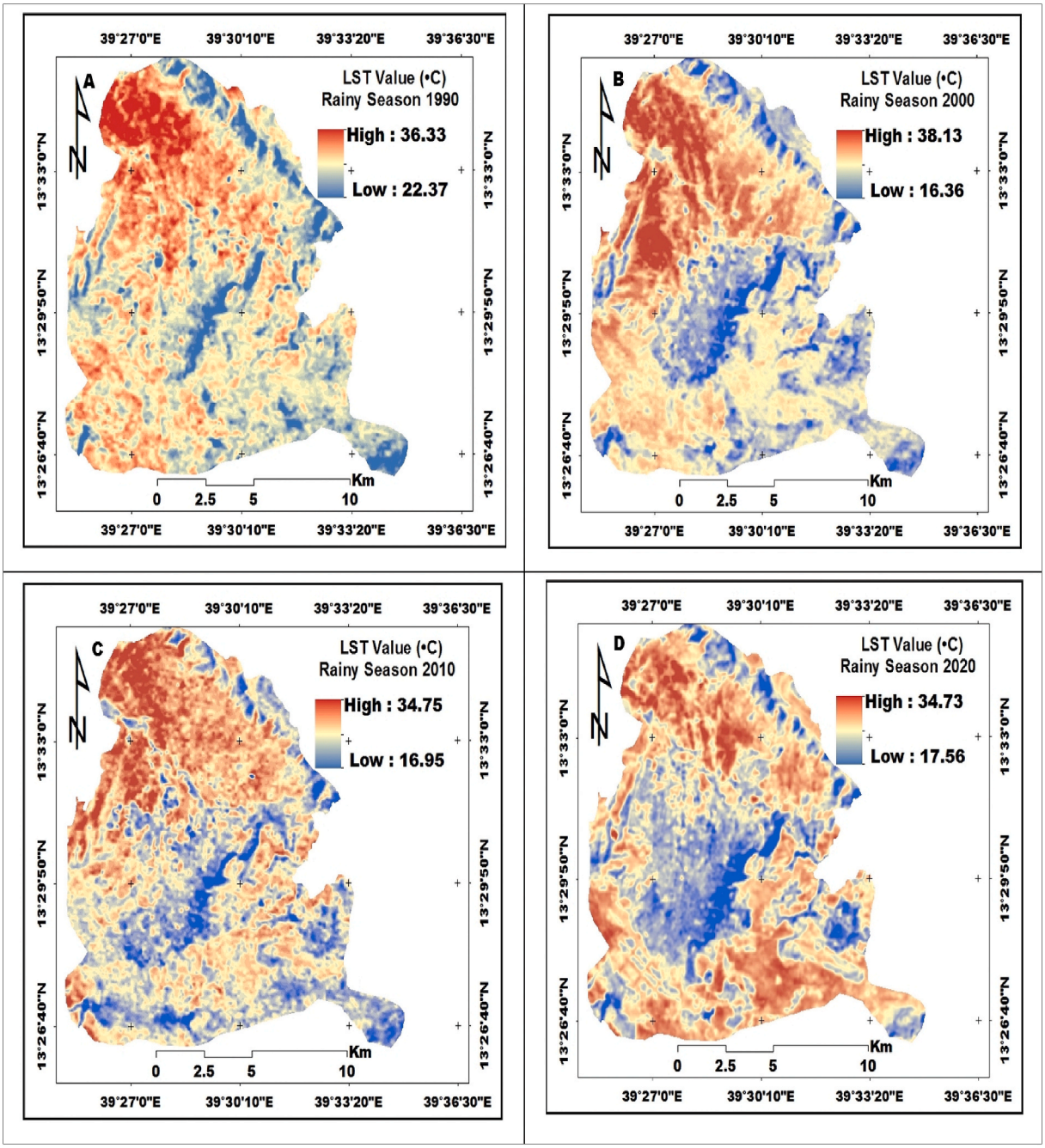

Fig. 7. - Rainy season average LST map (A) 1990, (B) 2000, (C) 2010 & (D) 2020.

decreased to 52.1% by 2020 (Table 13). Instead, considerable increases in both bright (+0.77%) and dark (+1.04%) impervious physical surfaces have been documented during the previous four decades (1990–2020). The city occupied around 1600 ha in 1984, 2304 ha in the early 1990s, 13,000 ha in 2005, and 19,682 ha now. Since 2005, the city's spatial growth pattern has expanded due to growing demand of land for housing, infrastructure, and enterprises. Urbanization plays an important role in the urban landscape [46] and has significant impacts on urban morphology as bare ground and vegetation are replaced by built-up areas. The result of our study is also consistent with the previous studies of [54].

In the 1990 wet seasons, dry bare land (Fig. 4) covered 85.2% of the urban land; however, by 2020, this proportion had declined significantly to 57.1% (Table 13), and the dry bare area) had also declined to 34.2% (Table 14) in the dry season of 2020, reflecting a net change of −0.39%. The construction of residential, industrial, and administrative structures at the expense of bare land is mostly to account for the alteration in the city's dry bare ground area. The city expanded mainly to the northeast (Semien sub city), northwest

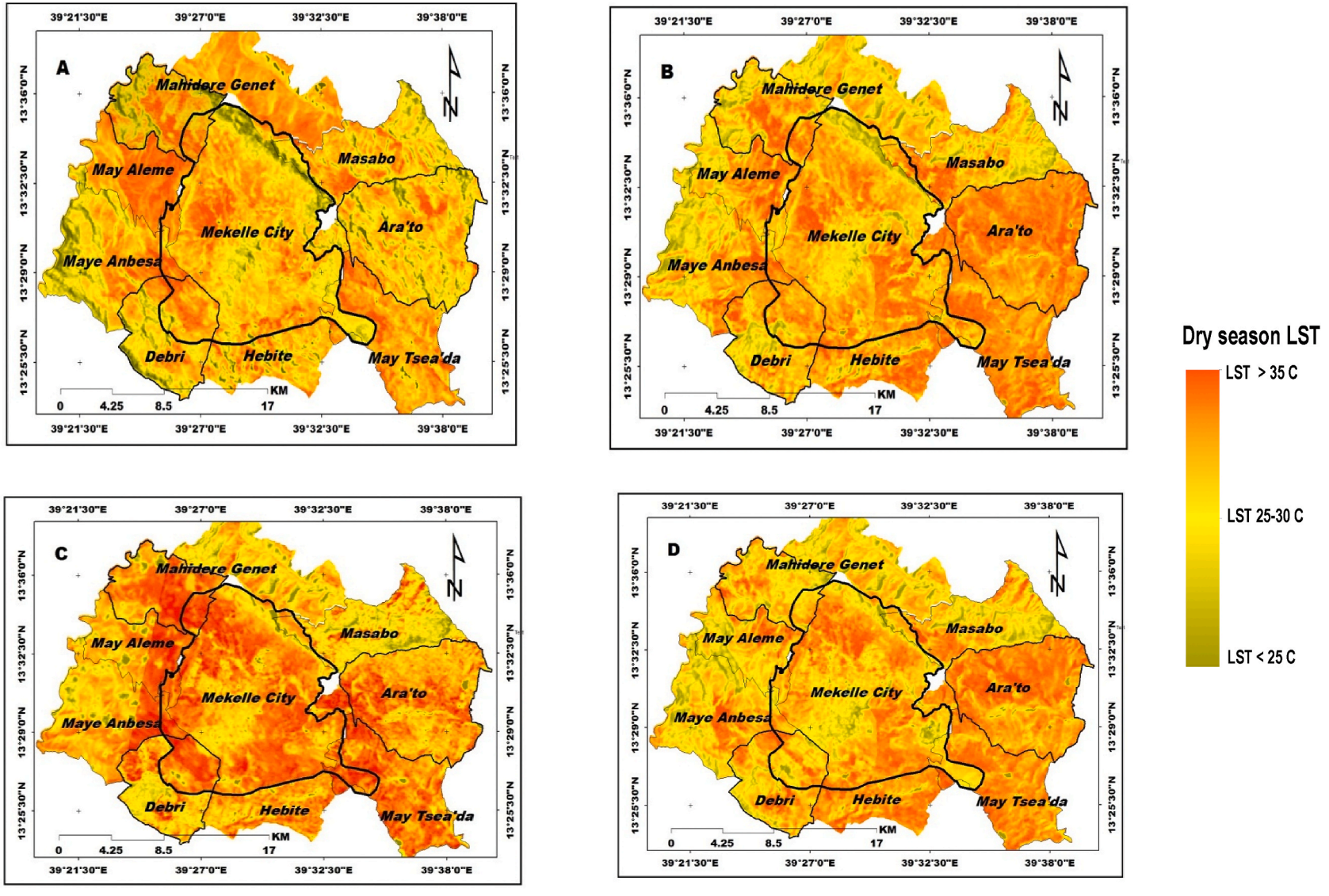

Fig. 8. Dry season LST Variation over Mekelle and Peripheral urban areas (A) 1990, (B) 2000, (C) 2010 & (D) 2020.

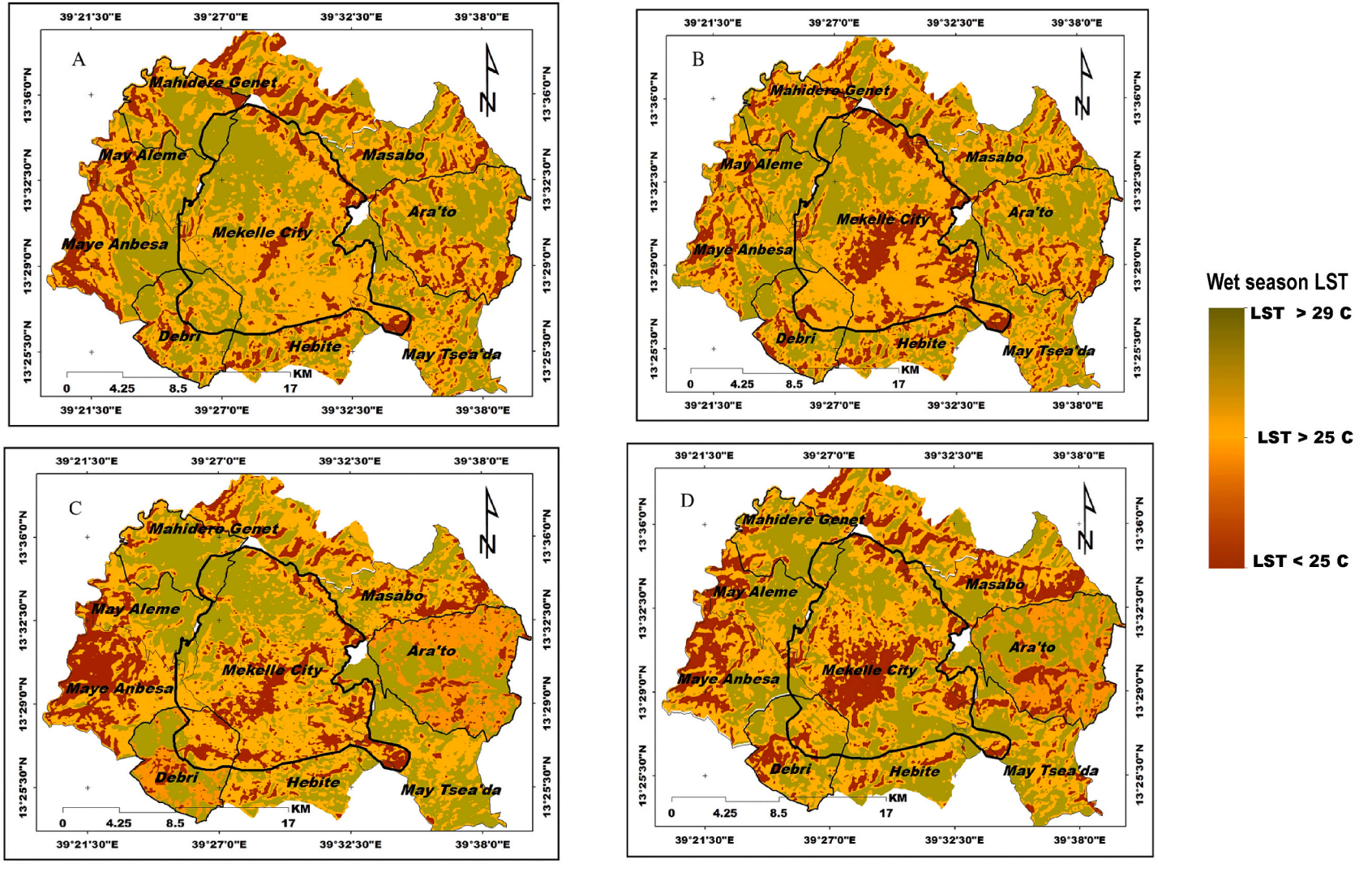

Fig. 9. Wet season LST Variation over Mekelle and Peripheral urban areas. (A) 1990, (B) 2000, (C) 2010, (D) 2020.

Table 17
Correlation between Variables (Dry season 1990–2020).

Correlations								
		LST	NDVI	BCI	DBSI	EBBI	MNDWI	DEM
Dry Season 1990								
LST	Pearson Correlation	1	−.111**	−.411**	.174**	.175**	−.148**	−.223**
	Sig. (2-tailed)		.000	.000	.000	.000	.000	.000
Dry Season 2000								
LST	Pearson Correlation	1	−.039**	−.275**	.457**	..372**	−.275**	−.061**
	Sig. (2-tailed)		.000	.000	.000	.000	.000	.000
Dry Season 2010								
LST	Pearson Correlation	1	−.186**	−.111**	.457**	.073**	−.107**	−.111**
	Sig. (2-tailed)		.000	.000	.000	.000	.000	.000
Dry Season 2020								
LST	Pearson Correlation	1	−.064**	−.072**	.440**	.503**	−.211**	−.248**
	Sig. (2-tailed		.000	.000	.000	.000	.000	.000
N = 213,139								

**. Correlation is significant at the 0.01 level (2-tailed).
LST (Land Surface Temperature), NDVI (Normalized Difference Vegetation Index), MNDWI (Modified Normalized Difference Water index), BCI (Biophysical Index), DBSI (Dry Bare Soil Index), EBBI (Enhanced Built-up Index).

Table 18
Correlation between Variables (Wet season 1990–2020)
Correlations.

		LST	NDVI	BCI	DBSI	EBBI	MNDWI	DEM
Wet Season 1990								
LST	Pearson Correlation	1	−.189**	−.162**	..374**	.199**	−.272**	−.286**
	Sig. (2-tailed)		.000	.000	.000	.000	.000	.000
Wet Season 2000								
LST	Pearson Correlation	1	−.395**	−.160**	.408**	.484**	−.436**	−.340**
	Sig. (2-tailed)		.000	.000	.000	.000	.000	.000
Wet Season 2010								
LST	Pearson Correlation	1	−.286**	−.016**	.139**	.411**	−.140**	−.317**
	Sig. (2-tailed)		.000	.000	.000	.000	.000	.000
Wet Season 2020								
LST	Pearson Correlation	1	−.213**	−.112**	.393**	.585**	−.468**	−.119**
	Sig. (2-tailed		.000	.000	.000	.000	.000	.000
N = 213,139								

**. Correlation is significant at the 0.01 level (2-tailed). .Note: *LST (Land Surface Temperature), NDVI (Normalized Difference Vegetation Index), MNDWI (Modified Normalized Difference Water index), BCI (Biophysical Index), DBSI (Dry Bare Soil Index), EBBI (Enhanced Built-up Index)*.
A standard multiple regression model was used to determine the causality and relative contributions of the independent factors (vegetation, impervious surface, dry bare soil, built-up, water bodies, and elevation) to determine the status of the dependent variable (LST) over the study area for the last forty years. The results of the dry season multiple standard regression models revealed that the impervious surfaces (BCI) was highly predicted by 16.8% of the variation with a standardized beta coefficient of −0.447 and the dry bare soil (DBSI) also slightly predicted by 3% of the variation with a standardized beta coefficient of 0.096 at a p-value of less than 0.001 the 1990s dry season LST.

(Ayder sub city), and southwest (Adi Haqi and Hadinet sub cities), since there was plenty of barren land available for residential and industrial regions. Our findings are similarly consistent with those of a previous study conducted by Ref. [54].

The extent of the built-up (Fig. 3) area has been gradually changing over the past forty years. Just 26% of the city was built-up in 1990, but by 2020, that number had increased to 50%, representing a net shift of +0.89% (Table 13). Urbanization has a significant influence on urban morphology and plays a significant part in the urban landscape as built-up regions replace bare ground and vegetation. The growth in residential, industrial, and administrative buildings is followed by an increase in population density, which is mostly to blame for the city's metamorphosis.

3.3. LST distribution over Mekelle city and adjacent rural districts

In this study, we examined the spatio-temporal pattern and distribution of LST in Mekelle and eight suburban districts that were in the same or nearly the same ecological zones as Mekelle. We measured the seasonal LST and sought into how they related to the size of the urban areas. The location, elevation, and land use of the suburban districts, including Mekelle city, are shown in Fig. 5.

The seasonal LST distribution map of Mekelle and peripheral districts (Tables 15 and 16) were derived from Landsat thermal bands (Eqs. (9)–(14)). The result reveals that Mekelle City's highest LST during the dry season was 46.53 °C in 1990 and reduced to 44.32 °C, 41.86 °C and 39.53 °C, respectively, in 2000, 2010 and 2020 (Fig. $6_{A\text{-}D}$). LST during the rainy season peaked at 36.33 °C in 1990, increased to 38 °C in 2000, then dropped to 35.8 °C and 34.7 °C, 2010 and 2020, respectively (Fig. $7_{A\text{-}D}$). In the 1990s, LST was highest

Table 19
Summary of coefficient of determination (Dry season 1990–2020).

Year	Model		Beta Coefficients		Statistics		Collinearlity Statistics	
			Unstad. B	Stand. B	T	Sig	Tolerance	VIF
1990	1	(Constant)	45.41		407.51	.000		
		NDVI (Vegetation)	−28.90	−.225	−116.26	.000	.856	1.169
		BCI (Impervious area)	−41.76	−.447	−225.12	.000	.813	1.230
		DBSI (Barren land)	3.72	.096	46.39	.000	.751	1.331
		EBBI (Built up area)	−3.66	−.128	−54.70	.000	.588	1.699
		MNDWI (Water)	−.06	−.272	−122.41	.000	.646	1.548
		DEM (Elevation)	−.00	−.188	−102.13	.000	.939	1.065
2000		(Constant)	20.67		196.38	.000		
	2	NDVI (Vegetation)	−.58	−.014	−8.59	.000	.996	1.004
		BCI (Impervious area)	−18.57	−.249	−128.01	.000	.725	1.380
		DBSI (Barren land)	14.69	.390	199.74	.000	.722	1.384
		EBBI (Built up area)	9.06	.287	117.06	.000	.457	2.186
		MNDWI (Water)	−.041	−.212	−86.84	.000	.463	2.160
		DEM (Elevation)	.000	.018	10.89	.000	.956	1.046
2010		(Constant)	37.97		528.37	.000		
		NDVI (Vegetation)	−20.70	−.438	−181.68	.000	.501	1.998
	3	BCI (Impervious area)	4.53	.063	32.73	.000	.786	1.272
		DBSI (Barren land)	33.93	.631	306.80	.000	.687	1.456
		EBBI (Built up area)	−1.78	−.095	−42.55	.000	.585	1.708
		MNDWI (Water)	6.299E-005	.039	14.50	.000	.400	2.498
		DEM (Elevation)	−.002	−.111	−64.99	.000	.990	1.011
2020		(Constant)	40.86		547.44	.000		
		NDVI (Vegetation)	−.005	−.255	−149.04	.000	−.253	.984
	4	BCI (Impervious area)	−.297	−.006	−1.906	.000	−.003	.289
		DBSI (Barren land)	.308	.012	5.279	.000	.009	.563
		EBBI (Built up area)	15.32	.332	113.83	.000	.194	.341
		MNDWI (Water)	12.38	.388	134.96	.000	.229	.350
		DEM (Elevation)	.000	.096	41.66	.000	.071	.549

a. Dependent Variable: 'Dry season LST 1990–2020. b. Predictors: (Constant), NDVI, BCI, EBBI, DBSI, MNDWI 1990–2020 & DEM. *(Note: Unstd. B = Unstandardized beta, Std B = Standardized beta, VIF = variance inflation factor). Source: own analysis via SPSS, 2020.*

in the city's northwestern portion, but it gradually shifted to the central and northeastern sections. This issue could be linked to the National Urban Planning Institute's (NUPI) growth plan, which was launched in 1991. The city grew further south and west as part of this new action plan [40].

The highest dry season LST (Fig. $8_{A\text{-}D}$) was recorded in 1990 in May-Alem (46.75 °C), May-Anbesa (46.38 °C) and Mekelle (46.38 °C). Mekelle, which has an urbanized environment, continues to have the highest LST intensity in 2000 (44.32 °C), 2010 (41.94 °C) and 2020 (39.53 °C). Mahidere Genet, which is located North of Mekelle city rose to second position in 2000 (38.13 °C) and 2010 (38.36 °C), then the maximum LST had increased to 40.21 °C in 2020 Fig. $8_{A\text{-}D}$). During the rainy season of 1990, the maximum LST was 46.3 °C in Mahidere Genet, 38.13 °C in Mekelle in 2000, and 37.5 °C and 36.04 °C in 2010, and 2020, respectively, in Mahidere Genet suburban area Fig. $9_{A\text{-}D}$). Between 2020 and 1990, all suburban cities had a negative net change in LST (Tables 15 and 16).

3.4. Relationship between LST and LULC

Pearson correlation matrices were conducted to examine the relation of the independent variables (vegetation, impervious surface, dry bare soil, built-up soil, water bodies, and elevation) in determining the status of the dependent variable (LST) seasonally for the past four consecutive decades. The assumptions of normality, linearity and homoscedasticity of variance were tested. This is also confirmed by (Table 20) the tolerance and variance inflation factor (VIF), which are well below the threshold of 0.10 and 10, respectively [55].

LST showed significant correlations during the dry season of 1990 (r ranging from −0.411** to 0.175** and $p < 0.01$). There was also a weak to moderate negative correlation with independent variables including NDVI (−0.111**), BCI (−0.411**), MNDWI (−0.148**), and DEM (−0.223**). In contrast, significant positive weak relationships were found between the dry season LST and key metrics including EBBI (0.175**) and DBSI (0.174**), which indicates that there is an increase in LST due to an increase of built up and barren land areas. Similarly to the previous study, LST also revealed a significant weak to moderate negative relationship with NDVI, BCI, MNDWI, and DEM in the years 2000, 2010, and 2020, with correlation coefficients of −0.039, −0.275, −0.275, and −0.061, respectively. On the other hand, built-up (EBBI) and dry lands (DBSI) were significantly ($p < 0.01$) correlated with the LST, and both showed a significant positive correlation with it, which indicated that a significant decline in the vegetation cover occurred as a consequence of the vast expansion of urban areas and infrastructure (Table 17).

The relationship between LST and urban LULC classes from the wet season was also examined in a similar way to that of the dry season. Table 18 shows that vegetation cover (r = −.189**), impervious surface (r = −0.162**), water bodies (r = −0.272**), and

Table 20
Summary of coefficient of determination (Wet season 1990–2020).

Year	Model		Beta Coefficients		Statistics		Collinearlity Statistics	
			Unstad. B	Stand. B	T	Sig	Tolerance	VIF
1990	1	(Constant)	.168		50.35	.000		
		NDVI (Vegetation)	−.719	−.206	−96.38	.000	.856	1.169
		BCI (Impervious area)	−.802	−.316	−144.03	.000	.813	1.230
		DBSI (Barren land)	.048	.045	19.92	.000	.751	1.331
		EBBI (Built up area)	−.066	−.085	−33.08	.000	.588	1.699
		MNDWI (Water)	−.001	−.174	−70.65	.000	.646	1.548
		DEM (Elevation)	.000	−.159	−78.03	.000	.939	1.065
2000		(Constant)	−.400		−116.49	.000		
	2	NDVI (Vegetation)	−.012	−.010	−5.52	.000	.996	1.004
		BCI (Impervious area)	−.396	−.183	−83.74	.000	.725	1.380
		DBSI (Barren land)	.321	.293	133.74	.000	.722	1.384
		EBBI (Built up area)	.230	.251	91.28	.000	.457	2.186
		MNDWI (Water)	−.001	−.177	−64.67	.000	.463	2.160
		DEM (Elevation)	1.696E-005	.023	12.15	.000	.956	1.046
2010		(Constant)	.023		10.14	.000		
	3	NDVI (Vegetation)	−.457	−.327	−124.56	.000	.501	1.998
		BCI (Impervious area)	.140	.066	31.39	.000	.786	1.272
		DBSI (Barren land)	.849	.536	238.77	.000	.687	1.456
		EBBI (Built up area)	−.028	−.051	−20.91	.000	.585	1.708
		MNDWI (Water)	2.190E-006	.046	15.67	.000	.400	2.498
		DEM (Elevation)	−4.681E-005	−.087	−46.63	.000	.990	1.011
2020		(Constant)	.202		81.04	.000		
	4	NDVI (Vegetation)	−.009	−.006	−1.68	.091	.289	3.459
		BCI (Impervious area)	−.014	−.018	−7.42	.000	.563	1.775
		DBSI (Barren land)	.372	.260	82.94	.000	.341	2.936
		EBBI (Built up area)	.337	.340	110.15	.000	.350	2.854
		MNDWI (Water)	2.943E-006	.055	22.17	.000	.549	1.821
		DEM (Elevation)	.000	−.226	−122.35	.000	.984	1.017

a. Dependent Variable: 'Wet season LST 1990–2020. b. Predictors: (Constant), NDVI, BCI, EBBI, DBSI, MNDWI 1990–2020 & DEM. (Note: Unstd. B = Unstandardized beta, Std B = Standardized beta, VIF = variance inflation factor). Source: own analysis via SPSS, 2020.

elevation ($r = -0.272^{**}$) relationships with wet season of LST in 1990, whereas both built-up regions ($r = 0.374^{**}$) and dry barren lands ($r = 0.199^{**}$) showed positive correlations and contributed statically significant at ($p < 0.01$) to the prediction of the LST. Similar to the preceding year's study, LST revealed a significant weak to moderate negative correlation with NDVI, BCI, MNDWI, and DEM [$r = -0.395^{**}$, -0.160^{**}, -0.436^{**}, and -0.340^{**}] in 2000, [$r = -0.286^{**}$, -0.016^{**}, -0.140^{**}, and -0.317^{**}] in 2010, and [$r = -0.213^{**}$, -0.112^{**}, -0.468^{**}, -0.119^{**}) in 2020 respectively. On the other hand, both built-up (EBBI) and dry lands (DBSI) showed a considerable positive correlation with the LST and were statically significantly ($p < 0.01$) contributed to predict LST (Table 18).

Similar to the preceding year's study, both the dry bare soil land classes (DBSI) and built up areas (EBBI) significantly predicted the status of the dry season LST in 2000, DBSI contributing for 20.8% of the variation with a standardized beta coefficient of 0.390 and EBBI also accounted for 13.8% of the variation with a standardized beta coefficient of 0.372 at a p-value less than of 0.001. The vegetation-covered areas also predicted the status of the dry season LST in 2010 and contributed 3.45% of the variation with a standardized beta coefficient of −0.438. In contrast, the dry bare soil land classes (DBSI) also significantly predicted the dry season LST status and contributed 20.8% of the variation with a standardized beta coefficient of 0.390, at a p-value less than of 0.001. However, during the same season of 2020, the standardized coefficient beta for EBBI (built up area) and DBSI (dry bare soil surface) demonstrated the highest value and contributed the most to the status of LST with a standardized beta coefficient of .332 (25%) and 0.012 (19%) uniquely predicted the dry season LST (Table 19).

The relative contributions of key factors (vegetation, impervious surface, dry bare soil, built-up soil, water bodies, and elevation) to determine the status LST from the wet season was also examined in a similar way to that of the dry season. The results of the multiple standard regression models revealed that the dry bare soil surfaces (DBSI) strongly predicted the wet season LST of 1990, with the standardized beta coefficient of 0.045, at a p-value less than of 0.001, and significantly determined by 13.98% of the variance of LST. Both open water bodies (MNDWI) and elevation (DEM) also slightly predicted the status of wet season LST at a p-value less than of 0.001, with the standardized beta coefficient of 0.174 and −0.159 and accounted for 7.39% and 8.17% of the variance LST, respectively. Furthermore, both the built up areas (EBBI) and vegetation-covered land classes (NDVI) also slightly predicted the wet season LST at a p-value less than of 0.001, with the standardized beta coefficient of 0.045 and −0.206 and contribute 3.96% and 3.57% to determine the variance of wet season LST of 1990s (Table 20).

Similar to the preceding year's study, both the built up areas (EBBI) and dry bare soil land classes (DBSI) significantly predicted the status of the wet season LST in 2000, the EBBI accounted for 23.42% of the variation with a correlation coefficient of 0.484 and the DBSI also accounted for 16.64% of the variation with a correlation coefficient of 0.408 at a p-value less than of 0.001. The vegetation-covered areas also significantly predicted the status of the dry season LST in 2010 and contributed 8.17% of the variation with a correlation coefficient of −0.286. In contrast, the built up areas (EBBI) also strongly predicted the dry season LST status and

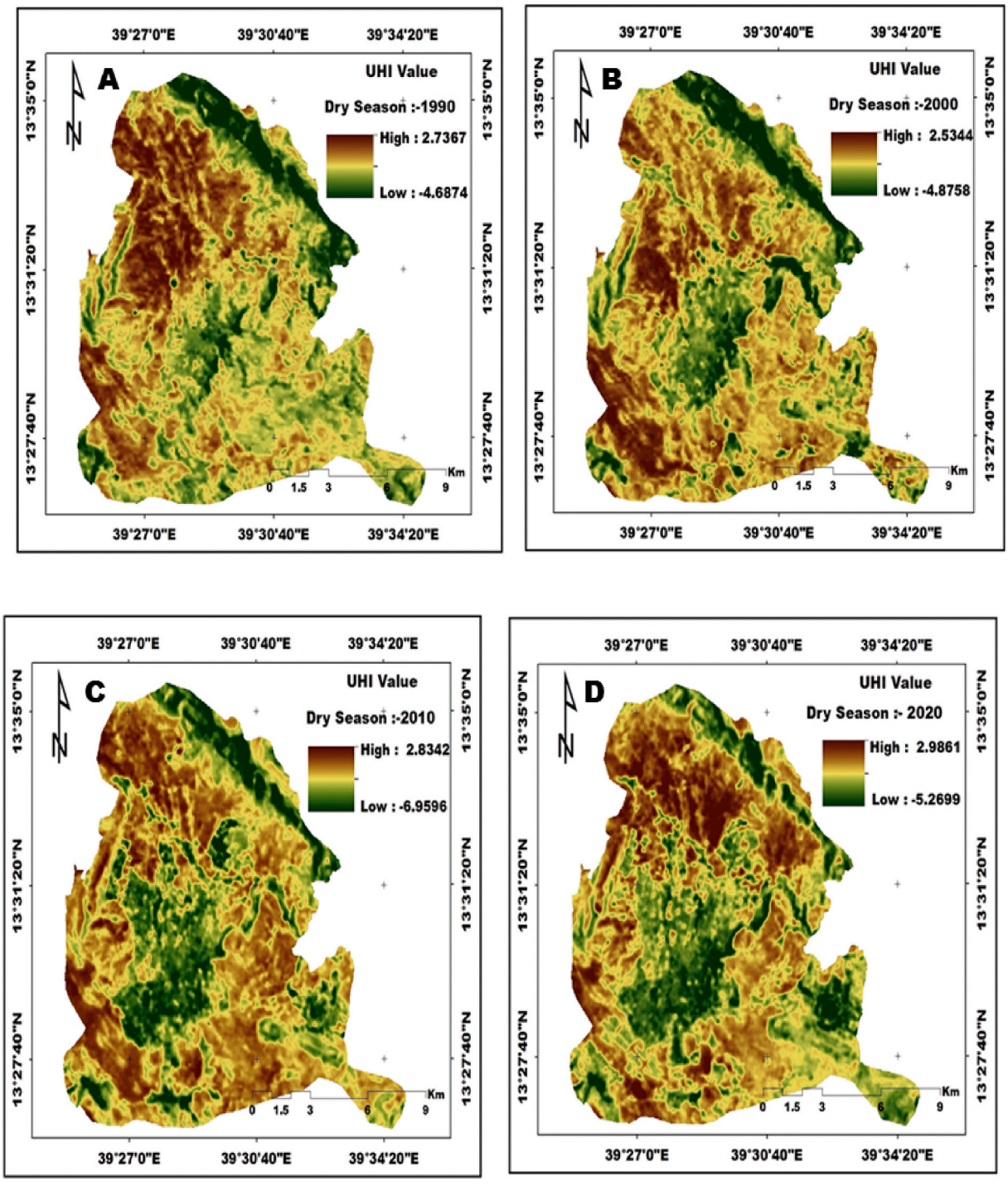

Fig. 10. Dry Season UHI map of Mekelle city (A) 1990, (B) 2000, (C) 2010, (D) 2020.

contributed 16.89% of the variation with; a correlation coefficient of 0.411, at a p-value less than of 0.001. However, during the same season of 2020, the standardized coefficient beta for EBBI (built up area) and MNDWI (open water surfaces) demonstrated the highest value and contributed the most to the status of LST with a correlation coefficient of .585 (34.22%) and 0.468 (21.9%) to determine the status of wet season LST (Table 20).

Table 21
UHI Variation over Mekelle city and Peripheral rural districts (Dry Season).

City/District	Dry Season UHI °C								Net Changes 2020–1990 (°C)	
	1990		2000		2010		2020			
	Max UHI	Min UHI	Max UHI	Min UHI	Max UHI	Min UHI	Max UHI	Min UHI	Δ Max UHI	Δ Min UHI
Arat'o	3.14	−4.52	3.69	−7.05	3.69	−7.61	2.58	−8.02	−0.56	−3.49
Debri	2.06	−3.41	2.79	−5.11	3.30	−4.05	2.61	−4.48	0.54	−1.06
Hebite *(Shibta)*	3.32	−5.52	2.28	−6.24	3.07	−7.10	2.96	−8.04	−0.35	−2.52
Masebo	2.58	−3.90	2.72	−3.98	3.72	−4.08	2.45	−3.44	−0.12	0.46
May Alem	2.34	−3.99	1.99	−4.15	0.76	−7.54	2.97	−3.83	0.63	0.16
May Tsea'da	2.79	−7.44	4.19	−6,33	2.36	−11.84	2.39	−8.05	−0.40	−0.61
May Anbesa	0.78	0.37	0.67	−2.43	0.70	0.40	2.83	−1.98	2.052	−2.35
Mahidere Genet	0.81	0.11	0.67	−2.43	0.80	0.41	2.99	−3.19	2.18	−3.3
Mekelle City	2.73	−4.68	2.53	−4.87	2.83	−6.95	2.98	−5.26	0.25	−0.57

N.B:- '**-** 'indicates decrease, '+' indicates increase in net Change rate.

3.5. Distribution pattern of UHI intensity over Mekelle city and adjacent rural districts

Based on the results of estimated seasonal UHI intensity (Equ.15), a maximum UHI value of 2.73 °C was recorded in Mekelle during the dry season in 1990, and it was also 2.53 °C, 2.83 °C and 2.98 °C in 2000, 2010 and 2020, respectively (Fig. $10_{A\text{-}D}$). In 1990, the highest UHI was recorded in the northwestern part of the city, which steadily shifted to the central and northeastern parts of the city. Meanwhile, minimum UHI of −4.8 °C, −4.87 °C, −8.95 °C and −5.26 °C was recorded in 1990, 2000, 2010 and 2020 respectively (Fig. $13_{A\text{-}D}$ & Table 21).

Similar to the dry season, maximum UHI of 3.23 °C was also recorded in the wet season of 1990 and 2.75 °C, 3.69 °C and 2.85 °C in 2000, 2010 and 2020 respectively (Fig. $11_{A\text{-}D}$). Meanwhile, minimum UHI of −5.99 °C, −4.32 °C, −5.95 °C and −4.37 °C in 1990, 2000, 2010 and 2020 was measured respectively. In the same season 2020 (Fig. $12_{A\text{-}D}$ & Table 22), Mekelle city recorded the highest UHI value (Max: 2.98 °C & Min: 5.26 °C), followed by Debri (Max: 2.61 °C & Min: 4.48 °C), Ara'to (Max: 2.58 °C & Min: 8.025 °C), Mesebo (Max: 2.45 °C & Min: 3.44 °C) and May Tsea'da (Max: 2.39 °C & Min: 8.05 °C). Several factors may contribute to this type of variation in UHI conditions, including urban development, geologic processes, anthropogenic heat, air pollution, and lower wind speeds [18]. One of the underlying assumptions for the variation in UHI status in Mekelle and the peripheral rural districts highly related to a notable expansion of impervious surfaces and a reduction in vegetation cover and water bodies.

3.6. The urban ecological effect of UHI in Mekelle city

The consequence of the gradual increase of LST leads to an increase of UHI [56,57]. The UTFVI can be used to describe the degree of vulnerability of urban residents to the effects of UHI. It was evaluated using the UTFVI, which is a widely used index to describe the effect of surface urban heat island (SUHI) with greater accuracy [37]. UTFVI concentration is higher when the area is significantly warmer than surrounding areas. The notable impacts of UTFVI include negative effects on local wind, humidity, air quality, reduction in comfort and increased mortality rate, indirect economic losses [38]. The map of seasonal UTFVI distribution was derived from LST and UHI and divided into six local UTFVI zones (None, Weak, Medium, Strong, Stronger, and Strongest) using the quintile approach (Figs. 14 and 15).

Fig. 14 shows the spatial pattern of UTFVI distribution in dry season in four different years from 1990 to 2020. The result shows that different impacts of UHI have been observed in Mekelle city over the last four decades and the city also has different types of thermal comfort zones. None thermal discomfort due to surface UHI effects (UTFVI <0.01) was observed in 57.32%, 48.21%, 50.82% and 54.92% of the city in 1990, 2000, 2010 and 2020, respectively. Similarly, 42.67%, 51.78%, 49.17%, and 45.08% of the city also noted thermal discomfort (UTFVI >0.01) and were affected by heat stress in 1990, 2000, 2010, and 2020, respectively (Table 23).

Similar to the dry season, in the wet season of 1990, 52.4% (10,226.6 ha) of the area was found to have an optimal microclimate (UTFVI <0), while in the same season of 2020, the area found to have an optimal microclimate decreased to 47.9% (9435.9 ha). In general, the result obtained by UTFVI showed that 51.9%, 55.7%, 51.97% and 52.2% of the city had no thermal discomfort due to SUHI effects (UTFVI <0.01) during the rainy season of 1990, 2000, 2010 and 2020, respectively. It was also found that 48.04%, 44.29%, 48.02% and 47.79% of the city experienced thermal discomfort and heat stress (UTFVI >0.02) to varying degrees during the rainy season of 1990, 2000, 2010 and 2020, respectively (Table 24).

3.7. Seasonal UTFVI variation over various urban land use classes

The UTFVI microclimate thermal zone and urban land cover class patterns were intersected to determine their mutual linkage. The result of this analysis revealed that; 71.5% (2514.3 ha), 89.5% (1411.6ha), 77.4% (2974 ha), and 78.6% (2878.7 ha) of the study area which is located with the vegetation covered area was recorded an optimal microclimate (UTFVI <0.01) in the dry season of 1990, 2000, 2010, and 2020 respectively (Table 25). While 52% (6832 ha), 62% (5441 ha), 67% (3056 ha), and 64.5% (6304 ha) of the study area which is covered with impervious physical feature (Table 26) was recorded thermal discomfort (UTFVI >0.01) microclimate in

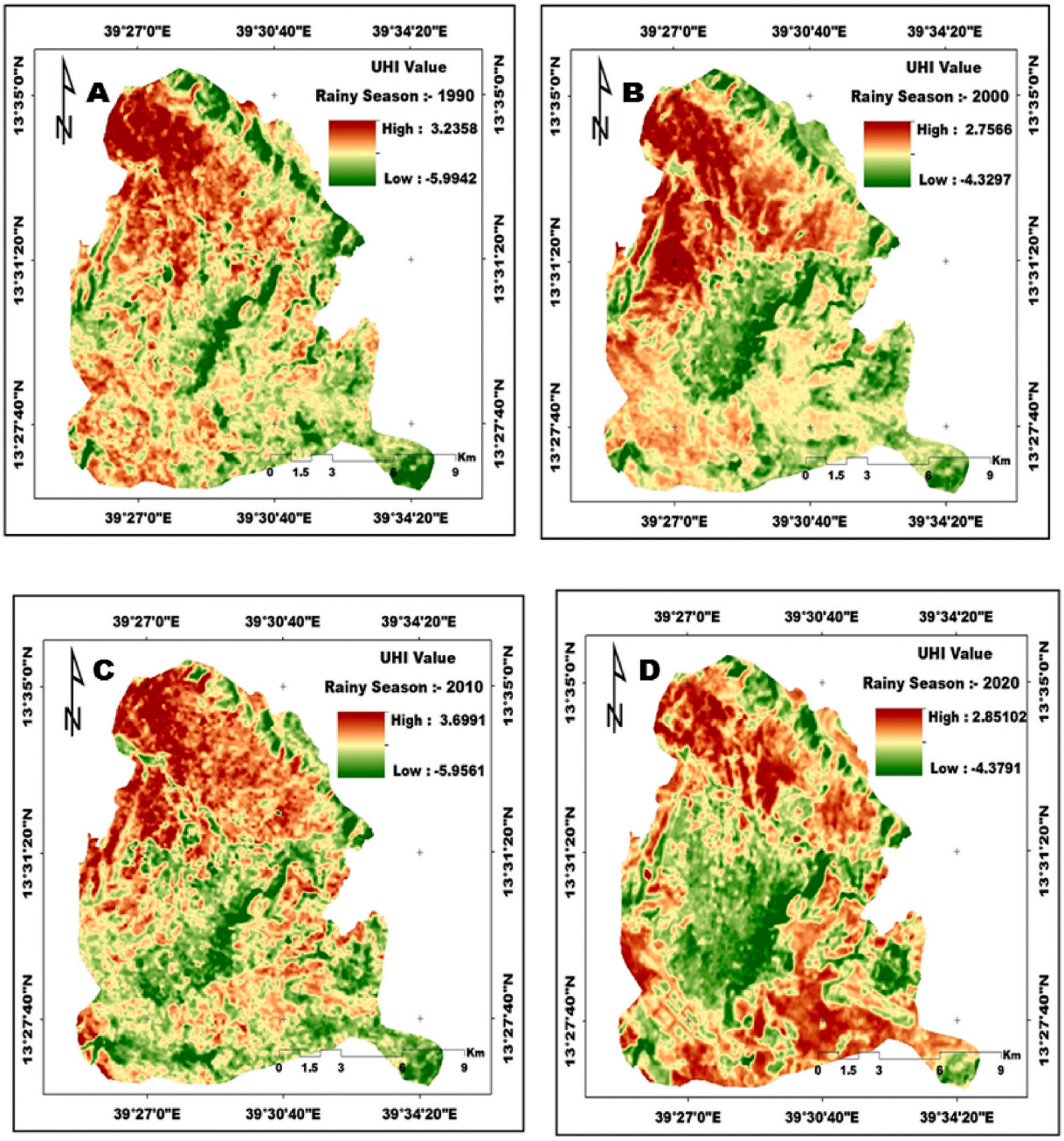

Fig. 11. Wet Season UHI map of Mekelle city (A) 1990, (B) 2000, (C) 2010, (D) 2020.

the dry season of 1990,2000, 2010, and 2020 respectively. Similarly, 29% (484 ha), 40% (2086 ha), 56% (4712 ha), and 56.3% (5566 ha) of built up areas (Table 27) and 54.9% (8716 ha), 69.5% (5729 ha), 58% (8755 ha), and 52.7% (8361 ha) of dry bare soil area (Table 28) was recorded thermal discomfort (UTFVI >0.01) microclimate in the same season of 1990,2000, 2010, and 2020 respectively.

Fig. 15 shows the spatio-temporal pattern of distribution, relationship, and variation of the thermal zone of the UTFVI microclimate during the wet season from 1990 to 2020. The results demonstrate that in 1990, 2000, 2010 and 2020, respectively, 78.9% (3371.92 ha), 90.3% (1597.6 ha), 74.7% (2688.9 ha) and 79.8% (6020.1 ha) of the land covered with vegetation (Table 29) had optimal microclimate (UTFVI 0.01). However, 42.6% (5525.4 ha), 41.5% (5438 ha), 27% (1249 ha), and 42% (4161 ha) of areas covered with impervious surface (Table 30), 29% (484 ha), 40% (2086 ha), 56% (4712 ha), and 56.3% (5566 ha) of built-up areas (Table 31) had a thermally uncomfortable microclimate (UTFVI >0.01) in the same season of 1990, 2000, 2010, and 2020, respectively. Similarly, 54.4% (8643 ha), 46.4% (5314 ha), 54.8% (8268 ha), and 55.6% (8830 ha) of urban areas with dry bare soil was recorded thermal

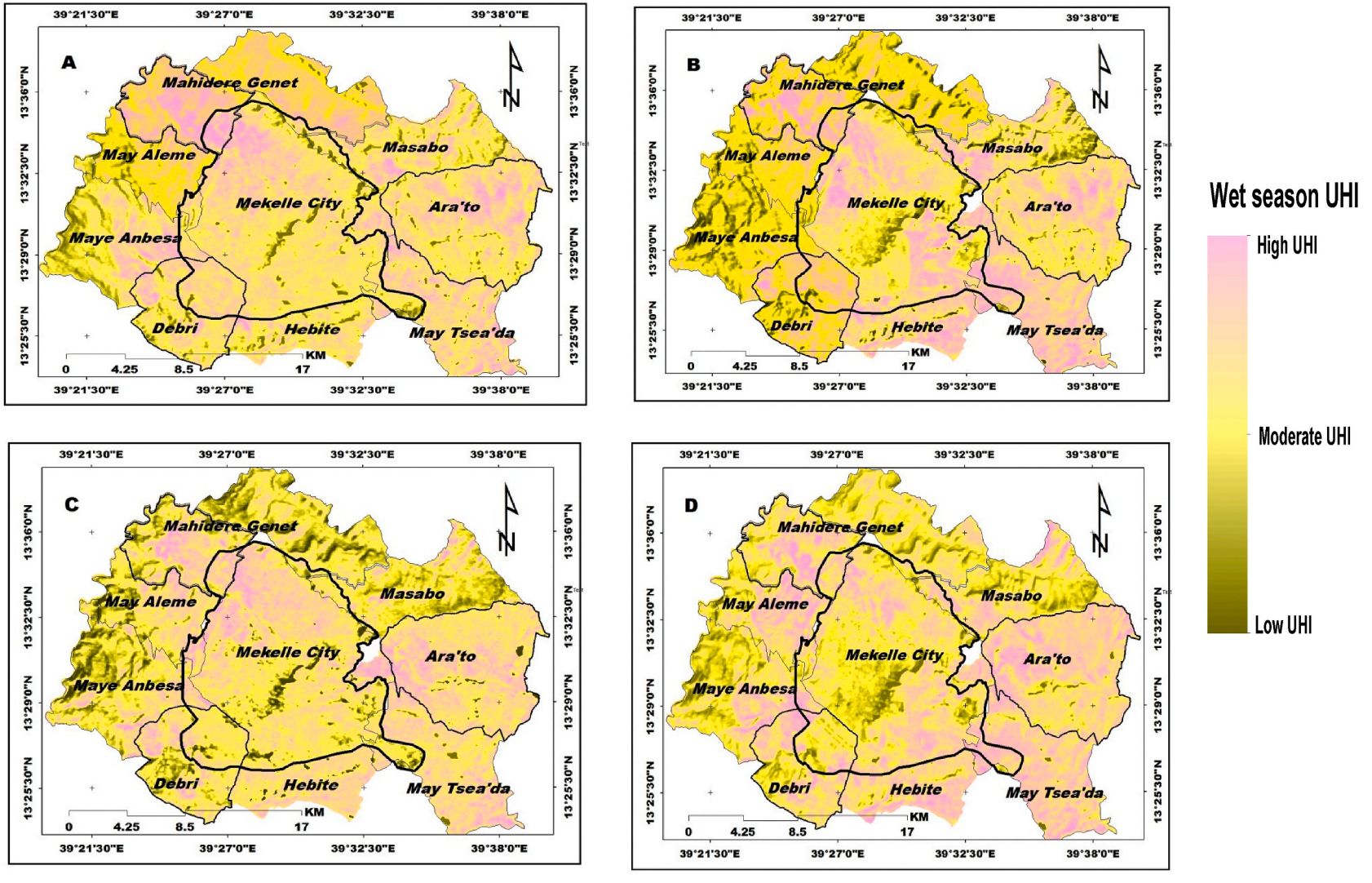

Fig. 12. Wet season UHI Variation over Mekelle and Peripheral urban areas. (A) 1990, (B) 2000, (C) 2010 (D) 2020.

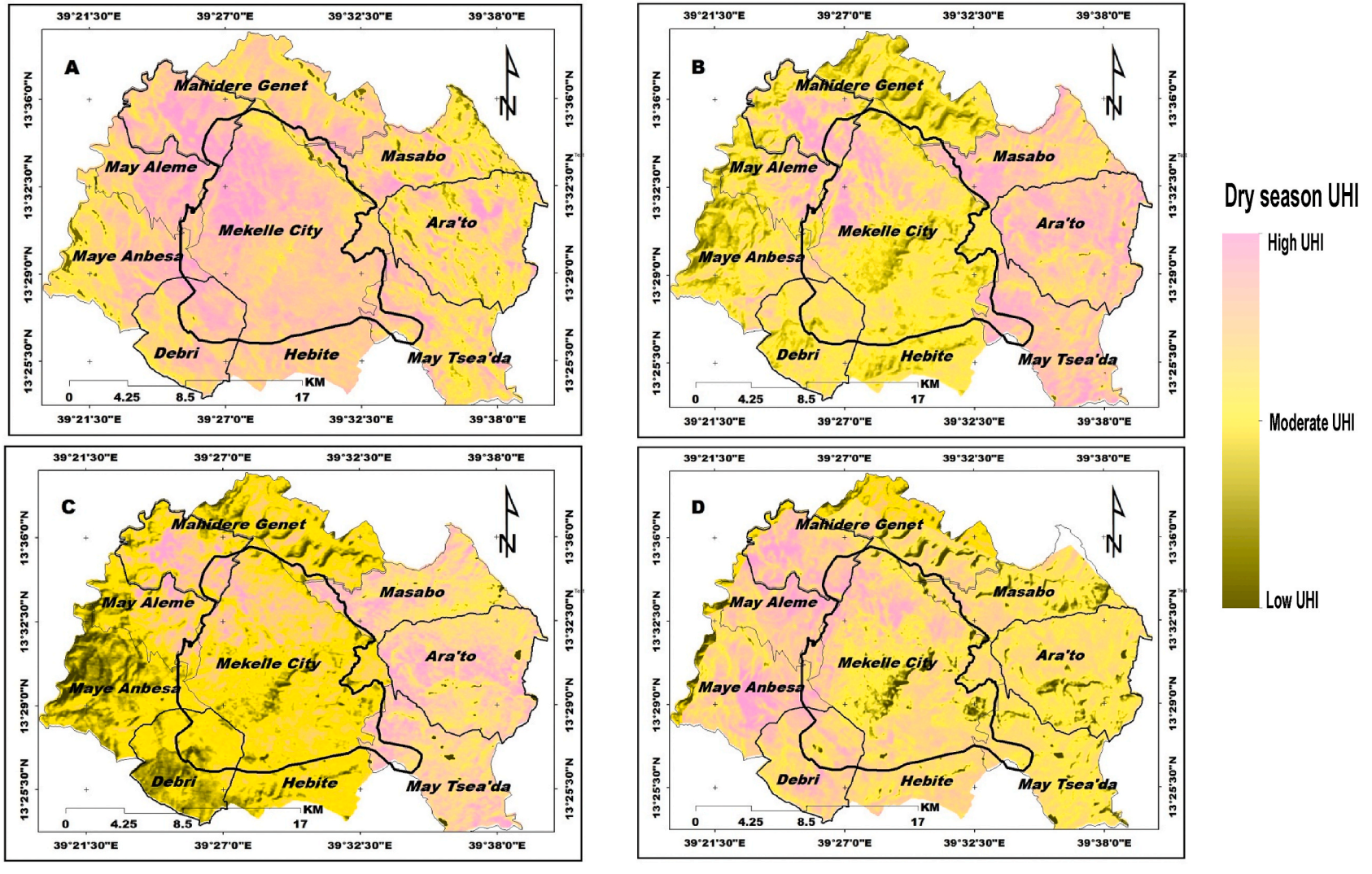

Fig. 13. Dry season UHI Variation over Mekelle and Peripheral urban areas (A) 1990, (B) 2000, (C) 2010, & (D) 2020.

Table 22
UHI Variation over Mekelle city and Peripheral rural districts (Wet Season).

City/District	Dry Season UHI °C								Net Changes 2020–1990 (°C)	
	1990		2000		2010		2020			
	Max UHI	Min UHI	Max UHI	Min UHI	Max UHI	Min UHI	Max UHI	Min UHI	Δ Max UHI	Δ Min UHI
Arat'o	2.91	−6.09	2.91	−6.09	3.69	−7.61	0.18	−0.54	−2.72	5.55
Debri	3.09	−5.24	3.09	−5.24	3.29	−4.04	0.27	−0.24	−2.82	5.01
Hebite *(Shibta)*	3.30	−5.58	3.30	−5.58	3.06	−7.08	0.24	−0.45	−3.06	5.13
Masebo	2.94	−4.65	2.94	−4.65	3.71	−3.77	0.20	−0.34	−2.74	4.31
May Alem	2.80	−4.32	2.80	−4.32	2.58	−3.99	0.28	−0.27	−2.51	4.05
May Tsea'da	3.19	−7.79	3.19	−7.79	3.99	−8.01	0.12	−0.51	−3.07	7.28
May Anbesa	0.78	0.37	1.93	−3.57	0.69	0.40	0.30	−0.24	−0.48	−0.61
Mahidere Genet	0.81	0.11	2.85	−3.92	2.85	−3.92	0.35	−0.28	−0.46	−0.39
Mekelle City	3.23	−5.99	2.75	−4.32	3.69	−5.95	0.28	−0.34	−2.95	5.65

N.B:- '**-** 'indicates decrease, '+' indicates increase in net Change rate.

discomfort (UTFVI >0.01) microclimate in the wet season of 1990, 2000, 2010, and 2020 respectively (Table 32).

4. Conclusion

This study investigated the impact of urban land use dynamics on the formation of UHI and its ecological effect (UTFVI) in Mekelle city from 1990 to 2020. The result of the study showed that a remarkable urban expansion was observed during the study period. It also leads to the loss of vegetation and the conversion of pervious areas into built-up and impermeable areas. As a result, urban areas are exposed to higher land surface temperatures compared to surrounding rural areas, which are referred to as an urban heat island (UHI).

The relationship between the independent variables (vegetation, impervious surface, dry bare soil, built-up soil, water bodies, and elevation) and the dependent variable (LST) seasonally over the previous four decades was analyzed using Pearson correlation matrices. The result reveals that NDVI, BCI, MNDWI, and DEM were independent factors with a negative linear correlation that contributed to keeping the earth's surface from getting extra radiation. Meanwhile, a positive linear correlation was observed between LST and the independent variables DBSI and EBBI. A standard multiple regression model was applied to ascertain the causality and relative contributions of the independent factors (vegetation, impervious surface, dry bare soil, built-up soil, and elevation), as well as the predictability status of the dependent variable (LST) over the study area for the past 40 years. The results of multiple standard regression models (in both seasons) revealed that the status of LST was significantly predicted and strongly contributed by the independent key variables such as of impervious surfaces (BCI), dry bare soil land (DBSI) and built up areas (EBBI). This finding indicate that the expansion of arid land surfaces, increased impervious infrastructure and built up areas due to expansion of urbanization are all contributing factors in variation of land surface temperature.

A trend analysis was also conducted to determine the UHI status of the city compared to seven selected peripheral suburban districts. The result showed that the UHI intensity of Mekelle city was relatively higher than that of the peripheral suburban districts especially in 2020 (both dry and wet seasons); this could be related to the remarkable urban land expansion. It is noteworthy that the study area affected by the urban heat island effect has increased during the study period, and for this reason, the study area has severe microclimate conditions mostly affect the quality of urban life and the worst conditions for thermal discomfort. More specifically, 36.2% (7124.8 ha), 44.3% (8719.9 ha), 41.3% (8133.2 ha) and 38.8% (7645.4 ha) of the area were affected by worse UHI effects (UTFVI >0.02) in 1990, 2000, 2010 and 2020, respectively.

The UTFVI microclimate thermal zone and urban land cover class patterns were intersected to determine their mutual linkage. During the dry seasons of 1990, 2000, 2010, and 2020, 17.8% (3512.9 ha), 8% (1575.6 ha), 19.5% (3849.8 ha), and 18.6% (3659.4 ha) of the area was covered with different vegetation types, respectively. At this time, 71.5% (2514.3 ha), 89.5% (1411.6 ha), 77.4% (2974 ha) and 78.6% (2878.7 ha) of the area had an optimal microclimate (UTFVI <0.01), while 28.4% (998.7 ha), 10.4% (164 ha), 22.7% (875.4 ha) and 11.72% (788.7 ha) of the area that was not covered with vegetation recorded thermal discomfort (UTFVI >0.01) in the same season of 1990, 2000, 2010 and 2020, respectively.

However, 47% (6111 ha), 37% (3304 ha), 32.8% (1496 ha), and 36.2% (3592 ha) of the area covered with impervious surface and 73% (1223 ha), 70% (3.694 ha), 45% (3666 ha), and 41.2% (4120 ha) of urban areas dominated by built-up areas respectively, registered thermal discomfort (UTFVI >0.01) in the local microclimate zone. In addition, thermal discomfort (UTFVI >0.01) was registered in 45% (7142 ha), 30.4% (2507 ha), 41.9% (6316 ha), and 47.2% (7497 ha) of the urban areas dominated by dry bare soil in the same season of 1990, 2000, 2010, and 2020, respectively.

Our results showed the influence of surface material on urban environmental cooling and heating by observing that high LST values were concentrated in built-up and low vegetated areas. The UTFVI index showed that the best thermal comfort was mainly associated with the presence of vegetation and open water bodies. Heavily built-up and industrial areas were the main places identified as UHI, the combination of materials with unfavorable thermal properties, such as concrete, and the extensive absence of vegetation in these locations contributes to the greatest impact of heat in these cases.

The contributions and purposes of green spaces and infrastructure have been considered in a number of national planning documents. These include Ethiopia's 1997 Environmental Policy and its 2015 Urban Greenery and Beautification Strategy, which aims to

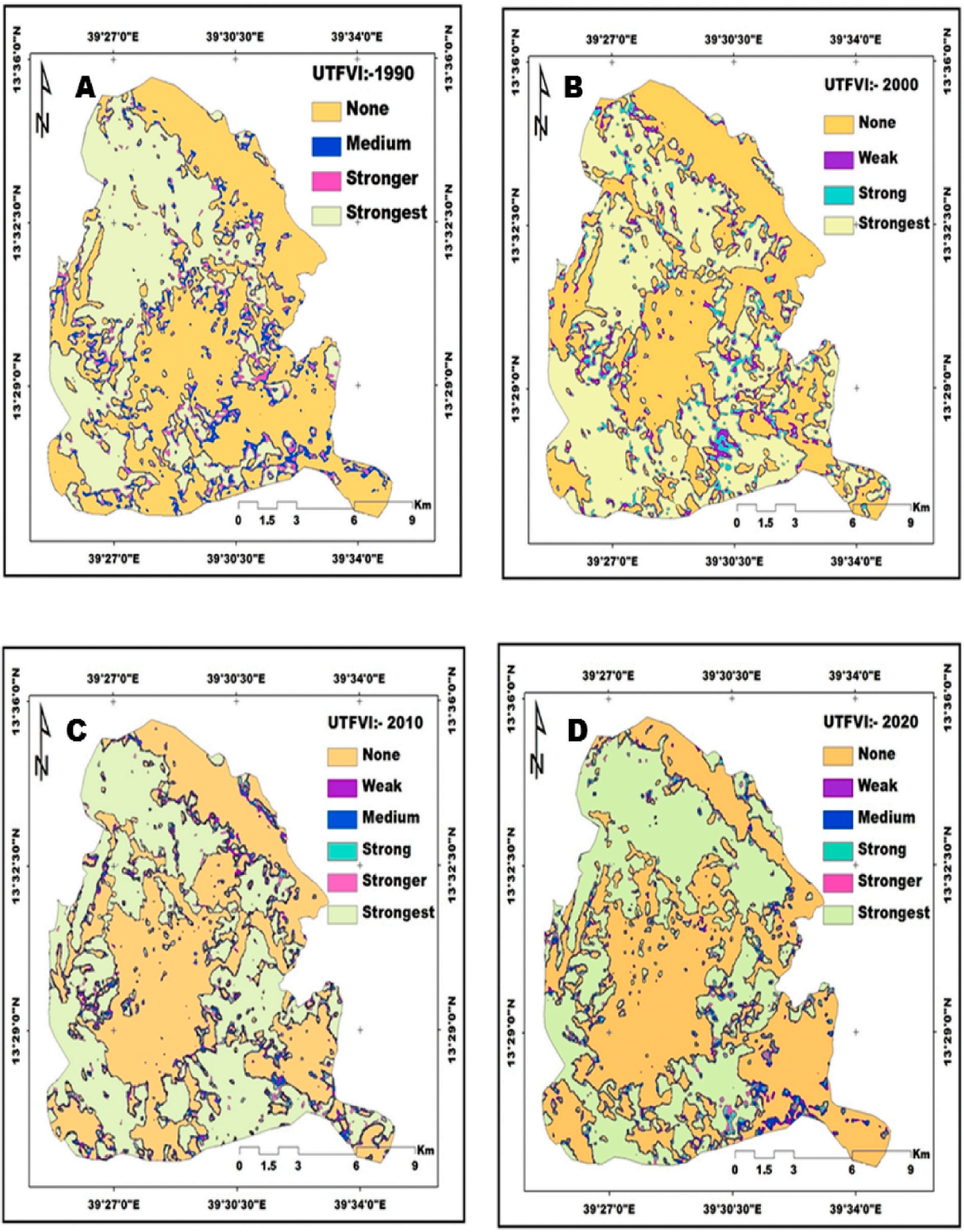

Fig. 14. Dry season UTFIV variation and distribution pattern map (A) 1990, (B) 2000, (C) 2010, & (D) 2020.

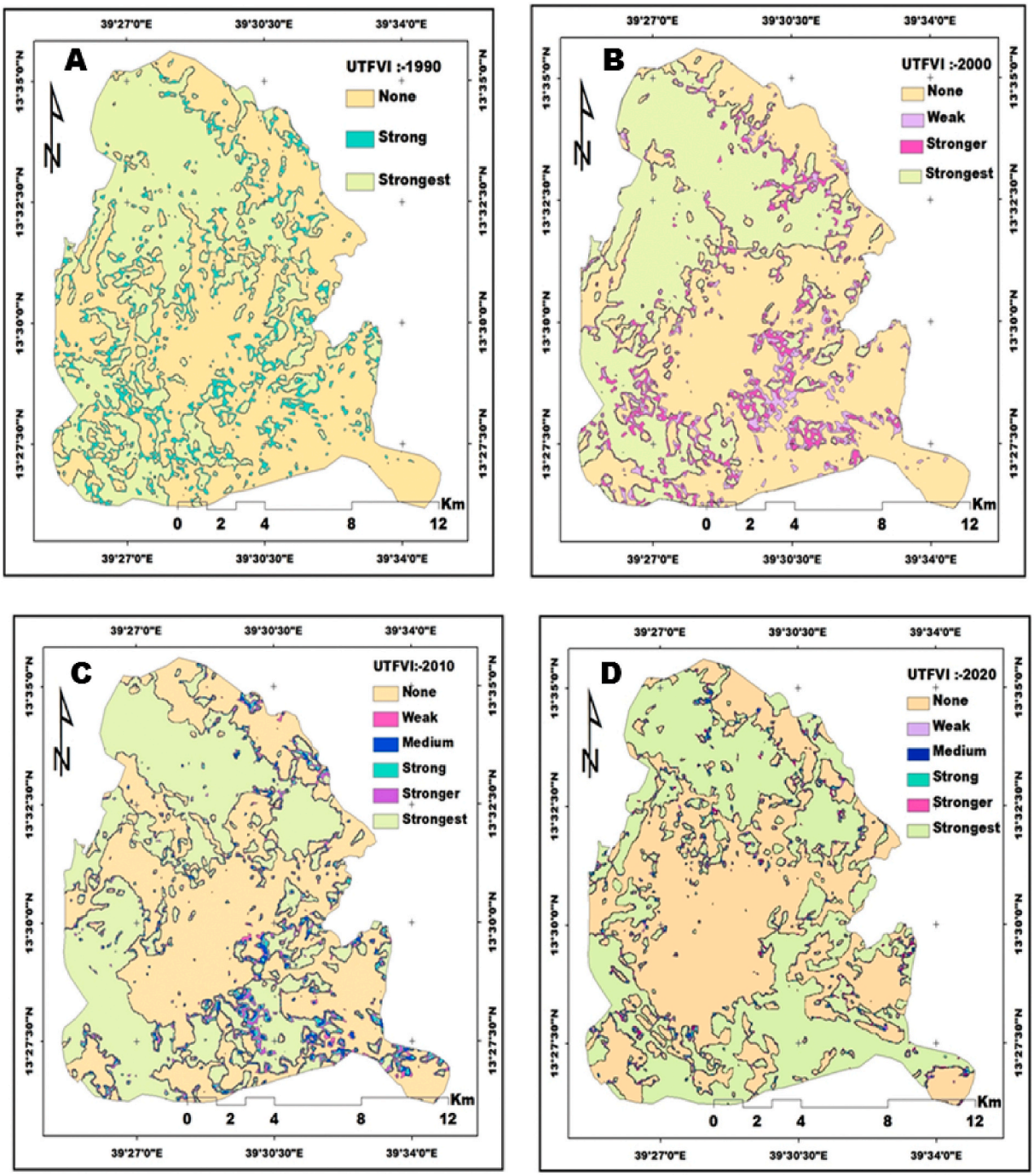

Fig. 15. Wet season UTFIV variation and distribution pattern map (A) 1990, (B) 2000, (C) 2010, & (D) 2020.

boost green spaces to prevent environmental deterioration, decrease the urban heat island effect, reduce runoff, and sequester carbon. The findings from this study provide valuable insights how inappropriate distribution and utilization of urban land use affects the urban environment and contributes to the emergence of UHI and thermal discomfort phenomena, both of which have a direct bearing on human well-being. To mitigate urban heat and build a sustainable urban environments, cities, and communities, policy makers and urban planners should take into account the effects of LST and UHI and integrate UHI comprehensive mitigation strategies with urban development patterns, construction material types, green infrastructure components, and current and projected local climate changes.

Table 23
Area (ha) distribution of UTFVI in the study Area.

Season	Year	None UTFVI (<0)	Weak UTFVI (0–0.005)	Medium UTFVI (0.005–0.01)	Strong UTFVI (0.01–0.015)	Stronger UTFVI (0.015–0.02)	Strongest UIFVI (>0.02)
		Area (ha)	Area (ha)	Area (ha)	Area (ha)	Area (ha)	Area (ha)
Dry Season	1990	9874.6	0	1408.1	0	1275.89	7124.8
	2000	8157.1	1332	0	1472.6	0	8719.9
	2010	8581.3	680.8	742.1	758.5	786.53	8133.2
	2020	9526.6	639.1	643.7	617.01	611.09	7645.4

Table 24
Area (ha) distribution UTFVI in the study Area.

Season	Year	None UTFVI (<0)	Weak UTFVI (0–0.005)	Medium UTFVI (0.005–0.01)	Strong UTFVI (0.01–0.015)	Stronger UTFVI (0.015–0.02)	Strongest UIFVI (>0.02)
		Area (ha)	Area (ha)	Area (ha)	Area (ha)	Area (ha)	Area (ha)
Wet Season	1990	10,226.6	0.0	0.0	1954.4	0.0	7501.2
	2000	9594.7	1371.2	0.0	0.0	1277.0	7441.1
	2010	9175.3	580.5	645.6	664.7	634.2	7983.3
	2020	9435.9	414.9	424.7	438.5	426.5	8542.8

Table 25
Distribution pattern and variation of UTFVI variation over LULC (Dry Season).

LULC Class	Year	None UTFVI (<0)		Weak UTFVI (0–0.005)		Medium UTFVI (0.005–0.01)		Strong UTFVI (0.01–0.015)		Stronger UTFVI (0.015–0.02)		Strongest UIFVI (>0.02)	
		Area (ha)	(%)	Area (ha)	(%)	Area (ha)	(%)	Area (ha)	(%)	Area (ha)	(%)	Area (ha)	(%)
Vegetation Cover	1990	2238.1	12.0	–	–	276.2	1.5	–	–	233.1	1.2	765.6	4.1
	2000	1352.5	6.9	59.2	0.3	0.0	0.0	50.6	0.3	0.0	0.0	113.4	0.6
	2010	2719.7	13.8	129.6	0.7	124.8	0.6	115.3	0.6	119.2	0.6	641.4	3.3
	2020	2641.3	13.4	118.4	0.6	119.0	0.6	107.1	0.5	95.44	0.49	578.14	2.9

Table 26
Distribution pattern and variation of UTFVI variation over LULC (Dry Season).

LULC Class	Year	None UTFVI (<0)		Weak UTFVI (0–0.005)		Medium UTFVI (0.005–0.01)		Strong UTFVI (0.01–0.015)		Stronger UTFVI (0.015–0.02)		Strongest UIFVI (>0.02)	
		Area (ha)	(%)	Area (ha)	(%)	Area (ha)	(%)	Area (ha)	(%)	Area (ha)	(%)	Area (ha)	(%)
Impervious Area	1990	5219.0	40.3	–	892.2	6.9	1.5	–	–	829.07	6.4	6003.2	46.6
	2000	2611.1	29.6	693	–	–	0.0	2720.6	30.8	–	–	2720.6	31.1
	2010	1183.8	26.0	160	152	3.4	0.6	1135.7	24.9	130.37	2.9	1790.1	39.3
	2020	3047.2	30.8	273	272	2.7	0.6	1260.2	12.7	1257.5	12.7	3786.6	38.3

Table 27
Distribution pattern and variation of UTFVI variation over LULC (Dry Season).

LULC Class	Year	None UTFVI (<0)		Weak UTFVI (0–0.005)		Medium UTFVI (0.005–0.01)		Strong UTFVI (0.01–0.015)		Stronger UTFVI (0.015–0.02)		Strongest UIFVI (>0.02)	
		Area (ha)	(%)	Area (ha)	(%)	Area (ha)	(%)	Area (ha)	(%)	Area (ha)	(%)	Area (ha)	(%)
Built up	1990	1148.3	6.2	–	–	75.52	0.4	–	–	71.44	0.4	368.14	2.0
	2000	3438.0	17.5	256.7	1.3	–	–	258.5	1.3	–	–	1255.3	6.4
	2010	3388.7	17.7	11.4	0.1	266.1	1.4	269.0	1.4	285.96	1.49	3861.9	20.1
	2020	3152.5	15.9	734.4	3.7	233.5	1.2	990.8	5.0	1326.2	6.7	3549.4	18

Table 28
Distribution pattern and variation of UTFVI variation over LULC (Dry Season).

LULC Class	Year	None UTFVI (<0)		Weak UTFVI (0–0.005)		Medium UTFVI (0.005–0.01)		Strong UTFVI (0.01–0.015)		Stronger UTFVI (0.015–0.02)		Strongest UIFVI (>0.02)	
		Area (ha)	(%)	Area (ha)	(%)	Area (ha)	(%)	Area (ha)	(%)	Area (ha)	(%)	Area (ha)	(%)
Dry Bare Soil	1990	5946.2	30.2	–	–	1196.6	6.1	2077.7	10.6	–	–	5638.8	33.7
	2000	2136.0	10.9	371.6	1.9	–	–	–	–	447.59	2.3	5281.5	26.9
	2010	5115.9	26.0	567.2	2.9	633.48	3.2	664.33	3.4	694.8	3.5	7396.4	37.6
	2020	6359.2	32.3	559.9	2.8	577.77	2.9	557.77	2.8	557.27	2.8	7246.4	36.8

Table 29
Distribution pattern and variation of UTFVI variation over LULC (Wet Season).

LULC Class	Year	None UTFVI (<0)		Weak UTFVI (0–0.005)		Medium UTFVI (0.005–0.01)		Strong UTFVI (0.01–0.015)		Stronger UTFVI (0.015–0.02)		Strongest UIFVI (>0.02)	
		Area (ha)	(%)	Area (ha)	(%)	Area (ha)	(%)	Area (ha)	(%)	Area (ha)	(%)	Area (ha)	(%)
Vegetation Cover	1990	3371.9	17.1	–	–	–	–	542.8	2.8	–	–	942.76	1.8
	2000	1494	7.59	33.76	0.17	–	–	–	–	25.1	0.1	100.86	0.5
	2010	2474.5	12.6	106.8	0.5	107.7	0.5	100.9	0.5	90.3	0.5	7,17.0	3.6
	2020	3803.3	19.3	171.2	0.9	2045.6	10.4	176.1	0.9	172.2	0.9	1169.6	5.9

Table 30
Distribution pattern and variation of UTFVI variation over LULC (Wet Season).

LULC Class	Year	None UTFVI (<0)		Weak UTFVI (0–0.005)		Medium UTFVI (0.005–0.01)		Strong UTFVI (0.01–0.015)		Stronger UTFVI (0.015–0.02)		Strongest UIFVI (>0.02)	
		Area (ha)	(%)	Area (ha)	(%)	Area (ha)	(%)	Area (ha)	(%)	Area (ha)	(%)	Area (ha)	(%)
Impervious Area	1990	5525.4	42.7	–	–	–	–	1314.1	10.2			6103.6	47.2
	2000	3853.1	29.5	1585.7	12.1	–	–	–	–	1534.6	11.7	6103.6	67.9
	2010	1023.4	22.5	108.9	2.4	117.4	2.6	114.05	2.5	98.91	2.2	3090.2	15.7
	2020	3748.3	37.9	201.9	2.0	211.1	2.1	215.50	2.2	207.5	2.1	5313.4	53.7

Table 31
Distribution pattern and variation of UTFVI variation over LULC (Wet Season).

LULC Class	Year	None UTFVI (<0)		Weak UTFVI (0–0.005)		Medium UTFVI (0.005–0.01)		Strong UTFVI (0.01–0.015)		Stronger UTFVI (0.015–0.02)		Strongest UIFVI (>0.02)	
		Area (ha)	(%)	Area (ha)	(%)	Area (ha)	(%)	Area (ha)	(%)	Area (ha)	(%)	Area (ha)	(%)
Built up	1990	1179.4	6.0	–	–	–	–	147.36	0.7	–	–	336.64	1.7
	2000	2926.0	14.9	195.3	1.0	–	–	–	–	179.8	0.9	1906.9	9.7
	2010	3164.3	16.3	216.1	1.1	227.5	1.2	224.7	1.2	202.0	1.0	4285.9	22.0
	2020	3052.5	15.7	1034.	5.3	233.5	1.2	1240.8	6.4	526.2	2.7	3799.4	19.5

Table 32
Distribution pattern and variation of UTFVI variation over LULC (Wet Season).

LULC Class	Year	None UTFVI (<0)		Weak UTFVI (0–0.005)		Medium UTFVI (0.005–0.01)		Strong UTFVI (0.01–0.015)		Stronger UTFVI (0.015–0.02)		Strongest UIFVI (>0.02)	
		Area (ha)	(%)	Area (ha)	(%)	Area (ha)	(%)	Area (ha)	(%)	Area (ha)	(%)	Area (ha)	(%)
Dry Bare Soil	1990	7216.0	36.7	–	–	–	–	–	–	2046.1	10.4	6597.0	33.5
	2000	2561.1	13.0	361.6	1.8	–	–	–	–	394.43	2.0	4920.0	25.0
	2010	5794.0	38.4	477.6	3.2	532.7	3.5	549.3	3.6	537.5	3.6	7181.3	47.6
	2020	6308.3	32.1	354.8	1.8	366.62	1.9	386.28	2.0	376.81	1.9	8066.9	41.0

Author contribution statement

Solomon Tesfamariam, Vanum Govindu and Abera Uncha. Conceived and designed the experiments; Performed the experiments; Analyzed and interpreted the data; Contributed reagents, materials, analysis tools or data; Wrote the paper.

Funding statement

This work was supported by Arba Minch and Mekelle University.

Acknowledgments

We would like to take this opportunity to thank Arba Minch University, Mekelle University, Mr Teshale Atsebha, Mr Mesfine Degaga, Mr Demelash Legesse, Mr Zelalem Bekele, and Mr Dawit Regassa for their continued and unreserved supports. We would also like to thank Editor-in-Chief and reviewers of this article for their critical observations and contribution.

References

[1] S. Kassahun, A. Tiwari, Urban development in Ethiopia: challenges and policy responses, IUP J. Gov. Pub. Pol. 7 (1) (2012) 59–65. Map of UHI (1990-2020).
[2] J. Ikerd, Beyond economic growth, J. Agric. Food Syst. Commun. Dev. (2014) 1. –3.
[3] R. Matthew, S. Chiotha, J. Orbinski, B. Talukder, Research note: climate change, peri-urban space and emerging infectious disease, Landsc. Urban Plann. 218 (2022), 104298.
[4] 2006 PASDEP, "Ethiopia : Building on Progress : A Plan for Accelerated and Sustained Development to End Poverty (PASDEP) Annual Progress Report 2006/07 Ministry of Finance and Economic Development (MoFED) Addis Ababa Table of Contents," 2007.
[5] J.A. Voogt, T.R. Oke, Thermal remote sensing of urban climates, Remote Sens. Environ. 86 (3) (2003) 370–384.
[6] H. Taha, Heat Islands and Energy, Encycl. Energy, 2004, pp. 133–143.
[7] A. Daniels, Incorporating domain knowledge and spatial relationships into land cover classifications: a rule-based approach, Int. J. Rem. Sens. 27 (14) (2006) 2949–2975.
[8] R.L. Wilby, Constructing climate change scenarios of urban heat island intensity and air quality, Environ. Plann. Plann. Des. 35 (5) (2008) 902–919.
[9] F. Yuan, C. Wu, M.E. Bauer, Comparison of spectral analysis techniques for impervious surface estimation using landsat imagery, Photogramm. Eng. Rem. Sens. 74 (8) (2008) 1045–1055.
[10] I. Olarewaju Oluseyi, M. Salihu Danlami, A. John Olusegun, Managing land use transformation and land surface temperature change in anyigba town, Kogi state, Nigeria, J. Geogr. Geol. 3 (1) (2011).
[11] Q. Meng, L. Zhang, Z. Sun, F. Meng, L. Wang, Y. Sun, Characterizing spatial and temporal trends of surface urban heat island effect in an urban main built-up area: a 12-year case study in Beijing, China, Remote Sens. Environ. 204 (2018) 826–837. November 2016.
[12] E. Teferi, H. Abraha, Urban heat island effect of Addis Ababa city: implications of urban green spaces for climate change adaptation, Clim. Chang. Manag. (2017) 539–552, 2017.
[13] Dagnachew Sisay, Tesfaye Korme, Understanding land surface temperature on rift areas to examine the spatial variation of urban heat island: the case of Hawassa, southern Ethiopia, Geojournal 86 (2) (2021) 993–1014.
[14] H. Tran, D. Uchihama, S. Ochi, Y. Yasuoka, Assessment with satellite data of the urban heat island effects in Asian mega cities, Int. J. Appl. Earth Obs. Geoinf. 8 (1) (2006) 34–48.
[15] C.J. Tomlinson, L. Chapman, J.E. Thornes, C.J. Baker, Including the urban heat island in spatial heat health risk assessment strategies: a case study for Birmingham, UK, Int. J. Health Geogr. 10 (1) (2011) 42.
[16] C.I. Portela, K.G. Massi, T. Rodrigues, E. Alcântara, Impact of urban and industrial features on land surface temperature: evidences from satellite thermal indices, Sustain. Cities Soc. 56 (October 2019) 2020.
[17] M. Babazadeh, P. Kumar, Estimation of the urban heat island in local climate change and vulnerability assessment for air quality in Delhi, Eur. Sci. J. 7881 (2015) 55–65. June.
[18] M.J. Hellman, M.S. Ramsey, Analysis of hot springs and associated deposits in Yellowstone National Park using ASTER and AVIRIS remote sensing, J. Volcanol. Geoth. Res. 135 (1–2) (Jul. 2004) 195–219.
[19] C.J. Merchant, Thermal remote sensing of sea surface temperature 17, 2013.
[20] H. Wang, Y. Zhang, J.Y. Tsou, Y. Li, Surface urban heat island analysis of shanghai (China) based on the change of land use and land cover, Sustain. Times 9 (9) (2017).
[21] C. Pathak, S. Chandra, G. Maurya, A. Rathore, M.O. Sarif, R.D. Gupta, The effects of land indices on thermal state in surface urban heat island formation: a case study on agra city in India using remote sensing data (1992–2019), Earth Syst. Environ. 5 (1) (2021) 135–154.
[22] J. Espinoza-Molina, K. Acosta-Caipa, E. Chambe-Vega, G. Huayna, E. Pino-Vargas, J. Abad, Spatiotemporal analysis of urban heat islands in relation to urban development, in the vicinity of the atacama desert, Climate 10 (6) (2022) 1–18.
[23] Q. Weng, Thermal infrared remote sensing for urban climate and environmental studies: methods, applications, and trends, ISPRS J. Photogrammetry Remote Sens. 64 (4) (2009) 335–344.
[24] O. Rozenstein, Z. Qin, Y. Derimian, A. Karnieli, Derivation of land surface temperature for landsat-8 TIRS using a split window algorithm, Sensors 14 (4) (2014) 5768–5780.
[25] D.P. Roy, et al., Landsat-8: Science and product vision for terrestrial global change research, Remote Sens. Environ. 145 (2014) 154–172.
[26] G.J. Roerink, Z. Su, M. Menenti, S.- SEBI, A simple remote sensing algorithm to estimate the surface energy balance, Phys. Chem. Earth - Part B Hydrol., Oceans Atmos. 25 (2) (Jan. 2000) 147–157.
[27] Z. Qin, A. Karnieli, P. Berliner, A mono-window algorithm for retrieving land surface temperature from Landsat TM data and its application to the Israel-Egypt border region, Int. J. Rem. Sens. 22 (18) (2001) 3719–3746.
[28] H. Benenson W, J. Harris, H. Stöcker, Lutz, Handbook Phys. 12 (12) (2002).
[29] A.M. Abdel-Ghany, I.M. Al-Helal, M.R. Shady, Evaluation of human thermal comfort and heat stress in an outdoor urban setting in summer under arid climatic conditions, Environ. Protect. Eng. 40 (3) (2014) 139–150.
[30] G.I. Cotlier, J.C. Jimenez, The extreme heat wave over western North America in 2021: an assessment by means of land surface temperature, Rem. Sens. 14 (3) (2022).
[31] H. Li, et al., Interaction between urban heat island and urban pollution island during summer in Berlin, Sci. Total Environ. 636 (2018) 818–828.
[32] Y. Zhu, S.W. Myint, D. Schaffer-Smith, R.L. Muenich, D. Tong, Y. Li, Formulating operational mitigation options and examining intra-urban social inequality using evidence-based urban warming effects, Front. Environ. Sci. 9 (2022) 1–16. January.
[33] A.W. Sejati, I. Buchori, I. Rudiarto, The spatio-temporal trends of urban growth and surface urban heat islands over two decades in the Semarang Metropolitan Region, Sustain. Cities Soc. 46 (2019), 101432. January.

[34] H. Li, Literature review on cool pavement research, Pavement Mater. Heat Isl. Mitig. (2016) 15–42.
[35] N. Torbick, M. Corbiere, Mapping urban sprawl and impervious surfaces in the northeast United States for the past four decades, GIScience Remote Sens. 52 (6) (2015) 746–764.
[36] T.S. Gala, R. Alfraihat, G. Mulugeta, T.S. Gala, Ecological evaluation of urban heat island in Chicago city, USA environmental monitoring view project GIS and public health view project ecological evaluation of urban heat island in Chicago city, USA, J. Atmos. Pollut. 4 (1) (2016) 23–29.
[37] A. Al Kafy, et al., Prediction of seasonal urban thermal field variance index using machine learning algorithms in Cumilla, Bangladesh, Sustain. Cities Soc. 64 (2021), 102542.
[38] M. Nuruzzaman, Urban heat island: causes, effects and mitigation measures - a review, Int. J. Environ. Monit. Anal. 3 (2) (2015) 67.
[39] X. Li, L.C. Stringer, M. Dallimer, The spatial and temporal characteristics of urban heat island intensity: implications for east africa's urban development, Climate 9 (4) (2021).
[40] N. Shimizu, A. Tesfay, R. Okazaki, E. Telele, R. Miyake, How has a local settlement urbanized in Mekelle, Ethiopia? Case of ïnda mesqel's development as one of the aspects of urbanization process, Ann. d'Ethiopie 32 (1) (2018) 213–242.
[41] U. Avdan, G. Jovanovska, Algorithm for automated mapping of land surface temperature using LANDSAT 8 satellite data, J. Sens. 2016 (2016).
[42] T.U. Omali, Ecological evaluation of urban heat island impacts in abuja municipal area of FCT abuja, Nigeria 7 (1) (2020) 66–72.
[43] B.N. Holben, Characteristics of Maximum-Value Composite Images from Temporal AVHRR Data, vol. 1161, 2007.
[44] H. Xu, Modification of normalised difference water index (NDWI) to enhance open water features in remotely sensed imagery, Int. J. Rem. Sens. 27 (14) (2006) 3025–3033.
[45] C. Deng, C. Wu, BCI: a biophysical composition index for remote sensing of urban environments, Remote Sens. Environ. 127 (Dec. 2012) 247–259.
[46] D. G, et al., Satellite and ground measurements for studying the urban heat island effect in Cyprus, Remote Sens. Environ. -Integr. Approach. 24 (2013) 1.
[47] A. Rasul, et al., Applying built-up and bare-soil indices from Landsat 8 to cities in dry climates, Land 7 (3) (2018).
[48] A.R. As-syakur, I.W.S. Adnyana, I.W. Arthana, I.W. Nuarsa, Enhanced built-UP and bareness index (EBBI) for mapping built-UP and bare land in an urban area, Rem. Sens. 4 (10) (2012) 2957–2970.
[49] A.A. Van De Griend, M. Owe, On the relationship between thermal emissivity and the normalized difference vegetation index for natural surfaces, Int. J. Rem. Sens. 14 (6) (1993) 1119–1131.
[50] S.M. Arafat, A. Darwish, INVESTIGATION of URBAN HEAT ISLAND USING by Conclusion References, 10th AARSE, 2014.
[51] G. Li, D. Lu, E. Moran, S. Hetrick, Mapping impervious surface area in the Brazilian Amazon using Landsat Imagery, GIScience Remote Sens. 50 (2) (2013) 172–183.
[52] Z. Su, The Surface Energy Balance System (SEBS) for Estimation of Turbulent Heat Fluxes, 2002.
[53] R.G. Pontius, M. Millones, Death to Kappa: birth of quantity disagreement and allocation disagreement for accuracy assessment, Int. J. Rem. Sens. 32 (15) (2011) 4407–4429.
[54] A.A. Fenta, et al., The dynamics of urban expansion and land use/land cover changes using remote sensing and spatial metrics: the case of Mekelle city of northern Ethiopia, Int. J. Rem. Sens. 38 (14) (2017) 4107–4129.
[55] A. Monroe, Multivariate statistics, Essentials Polit. Res. (2020) 173–208.
[56] A. Mohajerani, J. Bakaric, T. Jeffrey-Bailey, The urban heat island effect, its causes, and mitigation, with reference to the thermal properties of asphalt concrete, J. Environ. Manag. 197 (2017) 522–538. July 2017.
[57] J. Huang, et al., Simulation of thermal effects due to different amounts of urban vegetation within the built-up area of Beijing, China, Int. J. Sustain. Dev. World Ecol. 16 (1) (2009) 67–76.